

See discussions, stats, and author profiles for this publication at: <https://www.researchgate.net/publication/323738219>

Integrated Electromagnetic Wireless Power Harvesting System for mm-size Biomedical Implants

Thesis · April 2017

DOI: 10.13140/RG.2.2.32007.04000

CITATION

1

READS

2,030

1 author:



[Hamed Rahmani](#)

New York University

19 PUBLICATIONS 400 CITATIONS

SEE PROFILE

RICE UNIVERSITY

**Integrated Electromagnetic Wireless Power Harvesting
System for mm-size Biomedical Implants**

by

Hamed Rahmani

A THESIS SUBMITTED
IN PARTIAL FULFILLMENT OF THE
REQUIREMENTS FOR THE DEGREE

Master of Science

APPROVED, THESIS COMMITTEE:



Dr. Aydin Babakhani, *Chair*
Professor of Electrical Engineering, Rice
University



Dr. Behnaam Aazhang
Professor of Electrical Engineering, Rice
University



Dr. Caleb Kemere
Professor of Electrical Engineering, Rice
University

HOUSTON, TEXAS
APRIL 2017

ABSTRACT

Integrated Electromagnetic Wireless Power Harvesting System for mm-size
Biomedical Implants

by

Hamed Rahmani

Rising demand for continuous monitoring of human body and health care devices in recent years has resulted in the development of implantable biopotential sensors. Infection risks and mobility concerns constrain the implanted sensors to operate without any transcutaneous wire connection which raises serious challenges for powering and data telemetry. Lack of enough information on many physiological processes such as human speech production dynamics has hindered research on bases of the processes and it mainly stems from available measurement systems limitations.

In this work, we use electromagnetic waves in GHz frequency range to transfer the required power to the implanted system. The optimum frequency for wireless power transfer is studied as a function of transmitting and receiving antennas as well as the dispersive characteristics of the biological tissues. We present two types of power harvesting platform with on-chip antennas that can be integrated on a silicon chip. The first power harvesting system is designed to have a long-range operating range and harvests electrical energy from a far-field electromagnetic source and can be exploited to power up ultra-low power biomedical implants. The second system is designed to increase the functionality of a complex im-

plant such as a neural recording system. While maintaining the losses in biological tissues below Specific Absorption Rate (SAR) limit, the harvesting system can provide milliwatts of power the operation of a high performance fully integrated biomedical implant.

ACKNOWLEDGEMENTS

First, I would like to extend my sincere thanks to my advisor Prof. Aydin Babakhani for his infinite support, encouragement and for guiding me through all steps of my research. I am grateful to my committee members, Dr. Behnaam Aazhang and Dr. Caleb Kemere, and Dr. Aydin Babakhani for their careful and valuable examination and their advice that has fine-tuned this work.

I express my gratitude to my group-mates and my friends in Rice Integrated Circuits and Systems (RISC) group, Charles Chen, Mahdi Assefzadeh, Peiyu Chen, Himanshu Aggrawal, Babak Jamali, Yuxiang Sun, Seyed Mohammad Kazempour, Yaswanth Cherivirala, Dai Lee, Mahdi Forghani and Mostafa Hosseini. Especially, Babak for his guidance and support during early stages of my research.

Finally, I would like to thank my parents who have always encouraged me in my quest for higher education and their infinite love and support. I thank my sisters for believing in me and my goals. I thank my wife, Yasaman, for helping me through this work and her unconditional support. Her love and passion has always motivated me and brought happiness into our life.

Dedicated to the memory of my mother who is always in my heart.

Contents

Abstract	ii
Acknowledgements	iv
1 Introduction	1
2 Background	5
2.1 Near-Field Electromagnetic Power Transfer	9
2.2 Radiative Electromagnetic Wireless Power Transfer	12
3 Design Overview	15
3.1 A Power Harvesting Circuit for a High performance Biomedical Implant	17
3.2 A Far-Field Power Harvesting Circuit for an Ultra-low Power Biomed- ical Implantable Device	19
4 Wireless Link: Design and Characterization	20
4.1 Two-port Network Model	20
4.2 Power Efficiency	26
4.3 Multilayer Model of Tissue	28
4.4 Wireless Link Design	31
4.5 Power Harvesting System: Performance Evaluation	35
4.6 Specific Absorption Rate	40
5 Design of the Wireless Power Harvesting System Circuitry	44
5.1 Far-field Power Harvesting System	44

5.2	Radiative Near-field Power Harvesting System	50
5.3	Low-noise Amplifier	58
5.4	Performance Evaluation	60
6	Conclusion	64
	References	66

List of Figures

2.1	Implantable Devices	6
2.2	Brain Machine Interface	7
2.3	Electromagnetic Wireless Power Transfer	9
2.4	Electromagnetic Wireless Power Transfer	11
3.1	Conceptual Biomedical Implant	15
3.2	System Architecture of a Wireless Power Harvester for a High Performance Implant	17
3.3	System Architecture of a Far-Field Wireless Power Harvester	19
4.1	Power Flow in a Wireless Power Transfer System	22
4.2	Two port Network	23
4.3	Two port Network Circuit Model	25
4.4	Multilayer Model of Human Head	29
4.5	Biological Tissue Permittivity	31
4.6	Biological Tissue Permittivity	32
4.7	Receiving Antenna Used in the Radiative Near-field Power Harvesting System.	33
4.8	Simulation Configuration for The Far-field System	35
4.9	Simulated PTE of the Far-field Wirelss Power Harvesting System	36
4.10	Measurement Setup for Far-field Power Transmission System	37
4.11	Measured PTE of the Far-field Wirelss Power Harvesting System	38
4.12	Simulation Configuration for Radiative Near-filed power Harvesting System	39

4.13	Measurement Setup for Radiative Near-field power Harvesting System	40
4.14	Measured PTE of the Radiative Near-field System	41
4.15	Specific Absorption Rate at Different Frequencies	43
5.1	Dickson Voltage Rectifier	45
5.2	External Threshold Voltage Reduction	46
5.3	Threshold Compensated Multi-stage Dickson Voltage Rectifier	47
5.4	Matching Network	48
5.5	Micrograph of Fabricated Far-field Power Harvesting System	48
5.6	Measurement Setup for Evaluating the Performance of the Fabricated Power Harvesting System	49
5.7	Output Voltage of Far-field Power Harvesting System versus Transmit- ted Power Level	50
5.8	Block Diagram of PMU	51
5.9	Self-driven Voltage Rectifier	52
5.10	Equivalent Model of the Voltage Rectifier in Positive and Negative Operating Cycles	53
5.11	Input Impedance of the Designed Six-stage Voltage Rectifier	54
5.12	Circuit Schematic of the Mode-changing Unit	55
5.13	A Simple Reference Voltage Transistor	56
5.14	Circuit Schematic of the Voltage Regulator	57
5.15	A Conceptual View of Neural Signal Amplifier Array	58
5.16	Schematic of a Low-Noise Amplifier	59
5.17	Chip Micrograph of the Fabricated Radiative Near-field Power Har- vesting System	60
5.18	PMU Signals Waveform	62

List of Tables

2.1	Energy Sources	8
4.1	Optimum Frequency for Power Transmission into Biological Tissues .	21
4.2	Head Composition Tissue Thickness	30
5.1	Performance Summary of the Radaiative Near-field Power Harvesting System Circuitry	63
5.2	Performance Comparison of the Radaiative Near-field Power Harvest- ing System	63

Introduction

Recent advances in integration and semiconductor technology has led to the development of new systems and devices that are capable of operating inside the human body. Evolution of the biomedical implants in recent years has opened a new gate toward comprehending the mechanism of different psychological activities of human which may result in treating different disorders or restoring some mechanical of cognitive functions.

Although, research on the anatomical, physiological, and computational bases of more complex functions such as speech production has made important strides in recent years, but it has been limited by a glaring lack of information on the dynamics of the cognitive processes. This is a methodological limitation related to the low spatio-temporal resolution of widely available tools such as fMRI, EEG, behavioral, and stroke lesion based approach [1, 2]. At the current time, intracranial-electroencephalographic (icEEG) recordings in humans are carried out using either surface subdural grid electrodes (SDE) [3] or depth electrodes (DE) [4], both of which are designed for use in localizing seizures in patients with medically intractable epilepsy [4, 5, 6]. These recording systems have yielded valuable insights into the ultra-small structural scale at which phoneme production and decoding in humans

occurs [7, 8, 9, 10]. While such recordings provide excellent temporal resolution, the spatial resolution is optimized for current clinical needs and not for fine scale decoding of cognitive and motor processes. Additionally, the systems capable of recording at fine scales (e.g. Utah Array) are penetrating and connected to a recording system via cables that are external to the head, limiting patient mobility and providing a portal for central nervous system (CNS) infections [11]. The development of clinically applicable wireless solutions to overcome safety concerns and confounds have thus far been hindered by various following factors such as:

1. Power consumption by wide bandwidth Radio Frequency (RF) transmission
2. Miniaturization of electronics, power module, and connectors to allow for a low volume device
3. Design of an integrated system that allows for flexibility in the electrode array layout used for ECoG on a patient to patient basis
4. Long term stability and biocompatibility of encapsulation and electronics
5. Robustness of the device in real-world clinical settings incorporating the requisite technical parameters that are viable as a commercial.

Wirelessly powered implants can mitigate the serious issues that are related to infection risks and mobility of the patient. However, the operation of wireless implants is limited by the available power for the operation of a system. Development of a high-performance biomedical implant that can provide enough recorded data is strongly dependent on the available power.

Although using a battery for powering wireless systems is an easy solution, due to their bulkiness and limited lifetime they are not suitable for permanent implantable applications [12]. Instead, energy harvesting applications are good solutions which

are capable of providing a permanent energy source for the system and do not need bulky component such as a battery. Energy sources that can be used for this purpose are divided into two main categories [13].

1. Intrinsic energy sources such as body motion (Piezoelectric) [14], body temperature [15] and bio-potential [16]. In this category, power density is not enough to provide sufficient energy for implantable devices and they are not widely used in stimulating and wireless communicating biomedical applications [17].
2. External energy sources almost provide more power densities and are a better choice for multifunctional applications. The most common approach for power transferring for biomedical applications is using electromagnetic waves [18].

In this thesis, we present wireless power harvesting systems that are integrated on a silicon integrated chip. The design exploits on-chip antenna which can be implemented with the rest of the system and captures the incoming electromagnetic waves. The systems are miniaturized and highly integrated which make them appropriate for implanted applications. We introduce a new and novel power management technique that enables the mm-size designs to deliver enough power to a high-performance recording and transmitting system.

The remainder of this thesis is organized as follows: Chapter 2 reviews the current techniques for electromagnetic wireless power transfer and provides a background on the challenges of wireless power transfer to the implanted devices. In chapter 3, the design of power harvesting systems is discussed and a design overview is provided. In addition, the system architecture for each power harvesting system is described. In chapter 4, two-port network theory which is essential for wireless link analysis and calculation is presented; moreover, chapter 4 discusses the optimum frequency for wireless power transfer to the implanted systems through dispersive biological

tissues. In addition, tissue absorption is studied in order to make sure that the tissue absorption is below Specific Absorption Rate (SAR) limits which is set by Federal Communications Commission (FCC). Chapter 5 explains the details of the circuitry required for RF to DC conversion. A power management technique is introduced in this chapter that is implemented by a power management unit constituent of different analog sub-circuits. Design procedures and consideration of each sub-circuit are discussed. In addition, the performance of the system is characterized using both measurement and simulation tools. Finally, chapter 6 concludes this thesis.

Background

Biomedical implantable devices are widely used in today's medicine and play an important role in modern health care methods. Pacemakers, cochlear implants, deep brain stimulators, neuroPace, and retinal implants that are depicted in Figure 2.1 are some of the examples of the biomedical implants that help numerous patients who are suffering from different disorders.

Implanted devices are also greatly useful for sensing applications. Evolution of implanted sensing devices during past years has opened new gates toward research on human complex cognitive and sensory-motor functions.

Figure 2.2 shows an example of how a prosthetic arm can be controlled by recording and processing of neural activities. In this example, the signals are picked by the electrodes that are penetrated into the patient's brain. The signals are processed outside of the patient's head. The main features of the recorded signals represent different directions that the are targeted by the patient. The intended direction can be determined using different learning algorithm (such as Principle Component Analysis (PCA) or clustering). The prosthetic arm is moved to the intended direction then by applying proper command signals.

Exploiting fully implantable devices has vastly improved treatment methods by

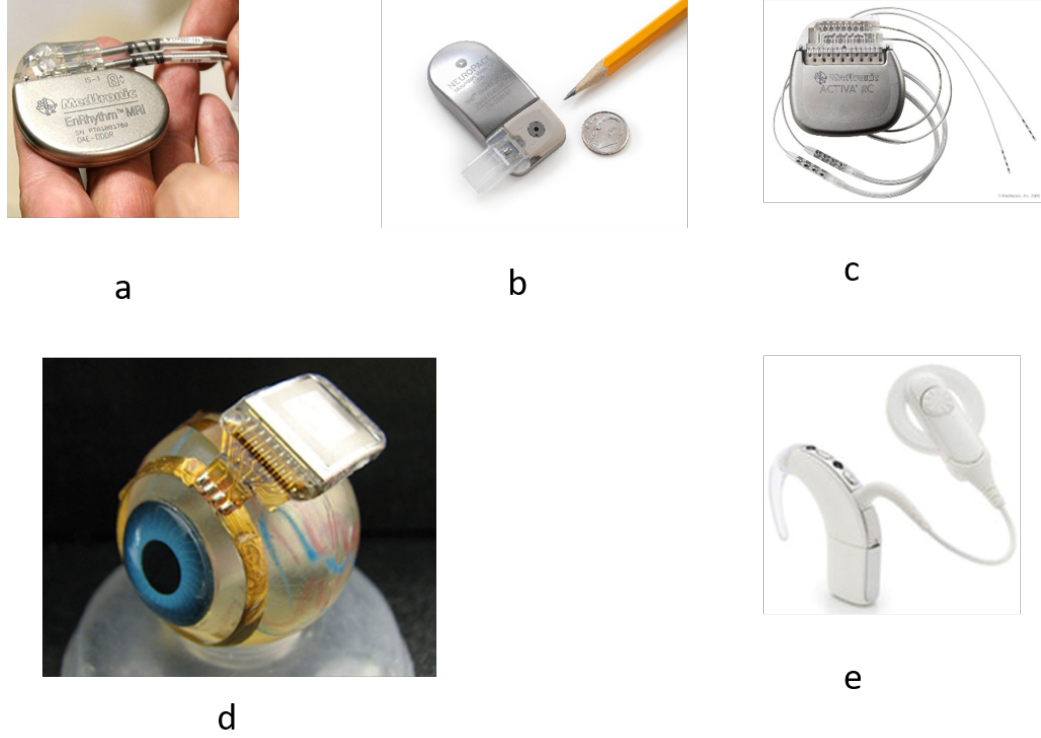


Figure 2.1: Some of the commercial biomedical implantable devices. (a). Cardiac Pacemaker (b) NeuroPace: Neurostimulator for preventing and controlling epilepsy (c) Deep-brain stimulator (d). Retinal prosthesis (e) Cochlear implant

enhancing patient monitoring and drug delivery techniques. Elimination of transcutaneous wire connection has made fully implantable devices popular since they alleviate infection risks and do not interfere with patient mobility.

Powering fully implanted devices is one of the serious challenges which dictated the functionality features such as processing power, communication bandwidth, the amount of recording channels. The amount of required power varies depending on the application. For instance, the required power for a pacemaker is $10 \mu\text{W}$ - 1 mW , while a retinal prosthesis requires about 45 mW . Although using batteries for ultra-low power implants seems a reasonable solution to power them, it is not a proper choice for powering the implants that require relatively high power. As an example, a pacemaker which consumes $8 \mu\text{W}$ can operate 10 years inside the patient's body

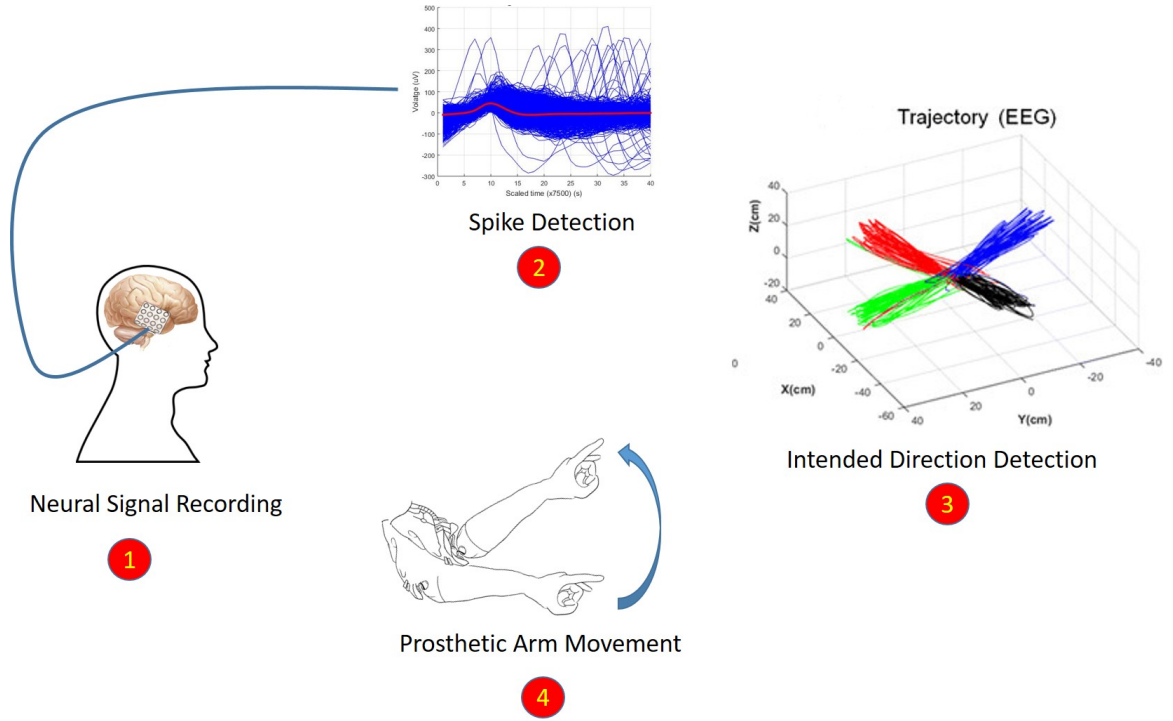


Figure 2.2: A conceptual view of a brain machine interface and the steps required for enabling a patient to move a prosthesis arm.

without any need of battery replacement, while a neural recording system with an average power consumption of 10 mW lasts only about 3 days [13]. In the case of neural implants, the replacement of the device requires a surgery and it makes no sense to use such a device with very limited lifetime. Another disadvantage of battery powered devices is the large area which is occupied by batteries. In some applications such as neural recording devices, integration is an important demand since it can potentially result in resolution improvement. Batteries cannot be integrated with the rest of implanted system and limit integration capability of those devices [19].

One solution for increasing the lifetime of the implanted devices is to design the electronics of the system with very stringent power consumption. Constituent electronic blocks should be designed with minimum power consumption. Another approach which is very popular among researchers is to utilize different energy sources that are available in implantable devices proximity and harvest the required energy

from the energy sources that are confined in the environment or created externally. Energy harvesting systems are capable of long-term operation are a very promising approach toward development of new and sophisticated systems. Sensing devices that harvest required power are emerging in particular for neural recording systems and neural simulators. Main energy sources that can be used for powering implantable devices are compared in Table 2.1 [13]. The energy sources can be divided into two main categories. Intrinsic energy sources that are available in body or surrounding environment of implanted devices usually provide low power densities and cannot be used for the applications with high power demand. However, these energy sources are still promising for ultra-low power applications and can eliminate batteries from the entire system. External energy sources generate a power stream from an external source to the implanted device using different carriers such as light, near-field coupling, far-field radiation, ultrasonic or acoustic waves [20].

Energy Source	Power Density
Temperature Gradient	$60 \mu\text{W}/\text{cm}^3$
Piezoelectric	$4 \mu\text{W}/\text{cm}^3$
Light	$100 \mu\text{W}/\text{cm}^2$ (office), $100 \text{mW}/\text{cm}^2$ (direct light)
Inductive Coupling	10mW (25cm^2) antenna size
Far-field Radiation	$1 \mu\text{W}$ at 10 cm with a 1.6 mm on-chip loop antenna.
Ultrasonic Transducer	$1.5 \text{mW}/\text{cm}^2$

Table 2.1: Comparison of different energy sources for powering energy harvesting implantable devices.

Electromagnetic energy transfer has been broadly used in the design of energy harvesting biomedical implants and has proven to be a reliable power transfer technique. Depending on the area constraints and safety limitations, EM powering can deliver μW to mW of power. Figure 2.3 shows the requirements of wireless power transmission using Electromagnetic waves. Electromagnetic wireless power transfer can be classified into different parts based on the operation frequency, structure, and

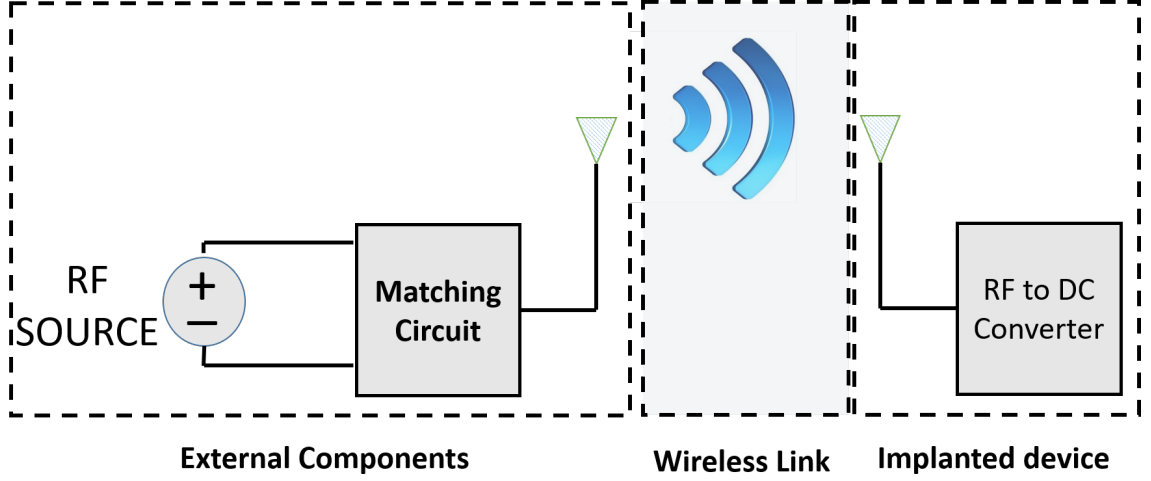


Figure 2.3: The building blocks of a wireless power transfer system.

working principles. Magnetic field coupling mode, electric coupling mode or electromagnetic radiation mode. In the rest of this chapter, we review wireless power transfer methods that are reported in the literature and provide a comparison between these two categories.

2.1 Near-Field Electromagnetic Power Transfer

There is no precise boundary division between different regions. However, the boundaries can be defined approximately based on the maximum dimension of an antenna and operating frequency. As an approximation, the area which is bounded by a circle with a radius of $0.62\sqrt{\frac{D^3}{\lambda}}$ is known as reactive near-field where D is the maximum dimension of the antenna and λ is the wavelength of transmitted electromagnetic waves. In this region, the E-field and H-field are out of phase by 90 degrees to each other [21].

In near field-region, E-field and H-field are not linked. Therefore, the power can be transferred using magnetic coupling between two coils or electric coupling between two metal plates. The fields in this region are not radiative which means that

energy stays at a close proximity of source and does not leave it if there is not any object to be coupled to the source. Magnetic field has been more popular for energy transfer through biological tissues since biological tissues show no magnetic properties and are transparent toward magnetic field. However, electric fields are also being researched and several systems have been developed that based on capacitive coupling [22, 23]. Inductive coupling systems operate in KHz to MHz frequency range. An Alternative Current (AC) goes through a transmitting coil (L_1) and induce another AC current in the receiving coil (L_2) according to Ampere's law. This causes creation of an electromotive Force (EMF) in the second coil which can drive a load connected to its terminals. Inductive coupling is the oldest power transfer technique which is commercially used in many implanted devices such as cochlear implants and pace-makers. The principle of operation of coupled system is researched and formulated in Couple mode theory [24]. Using the couple mode theory, an inductive coupling system can be represented with an equivalent circuit model as shown in Figure 2.4 [25]. R_S represent the internal resistance of the source and R_1 (R_2), L_1 (L_2) model intrinsic resistance and inductance of first (second) coil respectively while R_l shows load of the system. C_1 and C_2 can be used in order to tune the resonance frequency at both sides and increase the operation range of the system [26]. L_{12} is the mutual inductance between two coils. The mutual inductance depends on the geometry of coils and distance between them. Efficiency of an inductive near field system is strongly dependent on the mutual inductance and can be reported by coupling coefficient ($\kappa = \frac{M_{12}}{\sqrt{L_1 L_2}}$) which is a well-known figure of merit. Coupling coefficient is equal to the fraction of magnetic flux through L_1 that passes through L_2 . In order to achieve better power transfer efficiency, transmit and receive coils must be aligned and placed close to each other. In addition, enlarging the diameter of the coils boosts the transfer efficiency. In practice, inductive coupling systems use relatively large

coils and can achieve high efficiencies (70%). The operating range of these systems is limited by the size of the smaller coil and cannot be used in a situation where two coils are separated by a distance which is larger than 2-3 times of the smaller coil [27]. The operating range of inductive coupling systems can be increased using capacitors or self-resonance coils to form a resonant circuit at the primary and secondary side of the system at the same frequency. Although resonant inductive coupling systems can expand the operating range up to 10-times of the smaller coil dimension, they are still limited by the size of coils and require large coils to hold an acceptable operating range for biomedical applications. This fact limits the miniaturization of biomedical implants since, in a lot of applications such as deep neural stimulation, the area constraints prevent using a big coil for receiving power. On the other hand, efficiency of an inductive coupling system degrades dramatically when the separation between coils is large since the coupling coefficient of the system degrades and coils become weakly coupled. All of these factors cause inductive coupling method to fail for power transfer to miniaturized implants that are restricted in size and are implanted deep in tissue.

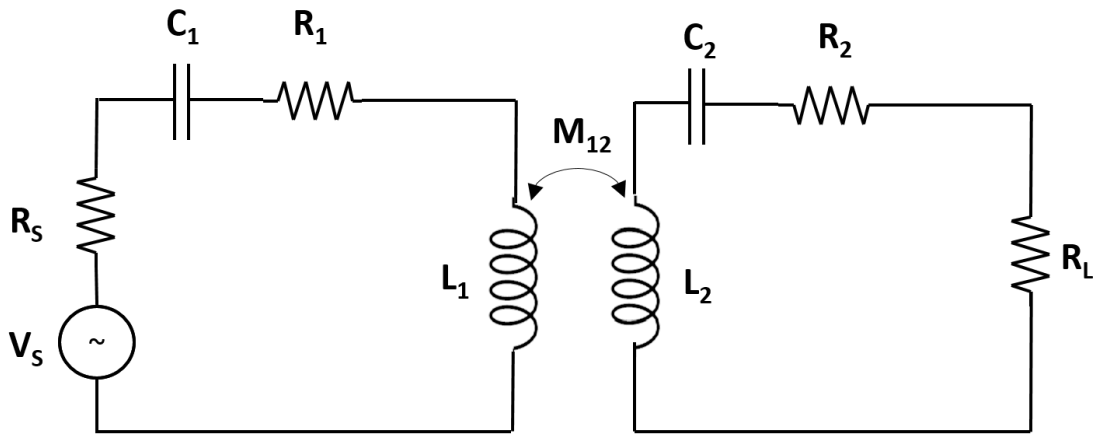


Figure 2.4: The building blocks of a wireless power transfer system.

2.2 Radiative Electromagnetic Wireless Power Transfer

Historically, wireless power transfer through biological tissues is done by inductive coupling technique in low-frequency range. Increasing the carrier frequency results in delivering more power since the rate of changes in incident magnetic field increases. Despite this fact, designers tended to use lower frequencies since it has less interaction with dispersive biological tissues and causes no tissue heating. This result was obtained assuming that there is no displacement current. This assumption leads to a diffusion equation which is a quasi-static approximation to Maxwell's equation. Solving the diffusion equation shows that higher frequencies decay faster inside tissue and have shorter penetration depth. Reference [28] claimed that the assumption of zero displacement current is only valid for perfect conductors and tissue is better to be modeled as a low loss medium. Solving Maxwell's equation without ignoring displacement current and taking frequency characteristics of tissues into account results that the optimum frequency for power transmission into biological tissues is at low-GHz frequency range. In the calculation done in [28] source is modeled as a magnetic or electric dipole and the optimum frequency is defined as the frequency which maximizes the ratio of delivered power to an implant over absorbed power by biological tissue.

Working in GHz frequency range could be beneficial in multiple ways. First, It makes it possible to miniaturize implanted devices since the size of the receiving antenna can be scaled by a factor of 100 compared to traditional inductive coupling systems. Second, it can potentially increase bandwidth of communication link between an external transceiver and the implanted device. These two features makes GHz frequencies desirable for wireless data transmission. As today's wi-fi is working in 2.4 GHz and

5 GHz carrier frequency and next generation wireless technology (5G) aims to even increase carrier frequency to 60 GHz to enable multi-Gbps data communication using mm-scale antenna arrays and GHz-scale available bandwidth [30, 29, 31].

Fully wireless implanted devices, need a communication link to transmit recorded data and receive control commands from an external transceiver. In some cases such as neural recording and stimulation, the amount of recorded data needed for a robust and real-time monitoring could be huge. For instance, in an experiment similar to Figure 2.2 that was done by Ohio State University and Battlle company, the required bandwidth for enabling hand movement is about 44 Mbps [32].

The electromagnetic waves carrying power can be modulated properly and convey the data as well that can be demodulated using an on-chip data demodulator [33]. High frequency communication systems provide high data bandwidth and Increasing frequency and miniaturizing size changes the filed-region when the separation between the antennas is in the order of few centimeter. In this situation, the transmit and receive antennas become weakly coupled or even have no coupling. Weakly coupled systems operate in radiative near-field region also known as midfield. In this region, the separation of antennas is comparable to the dimension of antennas. Once the distance between the antenna becomes large enough to eliminate coupling, the operation mode changes to Far-Field. Far-Field region is not widely used for power transmission to biomedical implants and is investigated for RFID applications mostly. The operation range can be extended using a power transmission method in far-field region. However, due to the attenuation caused by biological tissues and degraded antenna performance which is in a close proximity of tissues, a considerable amount of power is required at transmitting side in order to power up implanted devices.

An important issue which rises with development of implanted devices that use GHz frequency range is tissue absorption and heating effect. Any chronical heating in

living tissues is dangerous and can cause serious problems especially in the brain, the genitals, the eye, and stomach organs [34]. Different standards and metrics limit the exposure of human to electromagnetic waves. In the USA, The maximum allowable exposure limit for handheld devices such as cell phone which is set by Federal Communications Commission (FCC) 1.6 W/Kg averaged over 1g of tissue.

Design Overview

Neural recording and stimulation implants are one of the most challenging implantable devices to be designed. The reason is the sensitivity of brain tissue and importance of integration. Although, design consideration and limitations differs from application to application, most of the biomedical implantable devices have the same architecture. A conceptual diagram of a biomedical implant is in Figure 3.1.

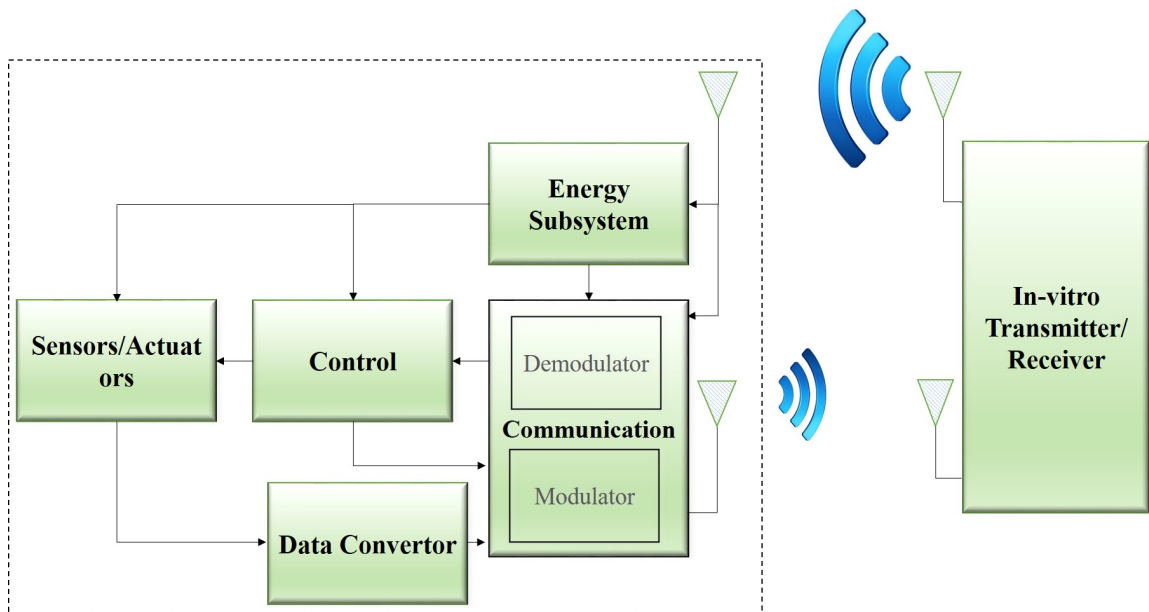


Figure 3.1: A conceptual block diagram of a typical biomedical implant used for recording and/or stimulation.

Usually, the functionality of the implants is limited by stringent power budgets. Therefore, post-processing on the recorded data is done externally. In this thesis, we aim to design a power harvesting platforms with two different focuses. First, a mm-size power harvesting subsystem that drives the block diagram of Figure 3.1. Particularly, we target neural recording devices since they are more challenging and a design for this application can successfully address the challenges in other application. Secondly, we target the implants that are ultra-low power. In this case, the design goal is to increase the operating range and use a far-field electromagnetic source to power up the implant. One of the main goals of this thesis is to design fully integrated systems that can be used in System on Chip (SoC) configuration. Therefore components including receiving antenna are designed on a single silicon chip in a standard CMOS technology. This eliminated any post-prepossessing and increase the reliability of the system. In addition, it facilitated mass production of implantable devices with a very low cost.

Maximum deliverable power without violating safety limits primarily determines the functionality of an implanted system. In order to increase the power budget, first we study the wireless link and the factors that impact the efficiency of power transfer efficiency. The energy subsystem includes an antenna which acts as a power receiver and picks incoming electromagnetic waves. It also has a voltage rectifier in order to convert RF signals to a DC voltage. Another part is the storage unit. Energy storage is another challenging task due to the limited area and compatibility with commercial CMOS processes.

Another approach to mitigate the problems raised by low power budget and functionality improvement is to design each block with stringent power limitation and include a power management unit in the system. Operating in GHz frequency range makes it possible to achieve charging times considerably faster than low-frequency biological

signals. Hence, using a power management technique can boost the functionality of the system by cutting off unnecessary power consumption and turning off some of the blocks are shown in Figure 3.1.

3.1 A Power Harvesting Circuit for a High performance Biomedical Implant

In this section, I describe system architecture of a biphasic power harvesting system that can drive the building blocks of the system shown in 3.2

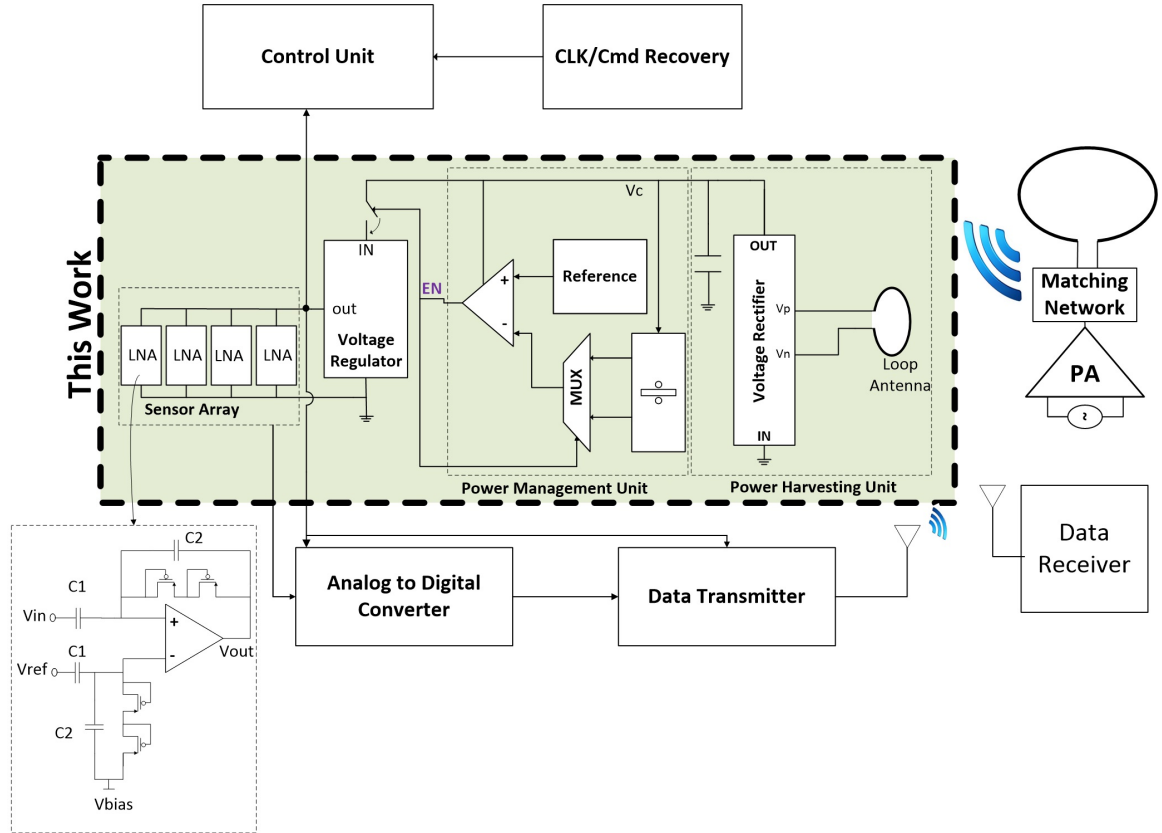


Figure 3.2: System architecture of a wireless power harvester for a high performance implant.

The power which is limited by safety regulations is transmitted by an external radiator while the power harvesting system is placed few centimeters away from the

TX antenna covered by layers of biological tissue. Received power by the antenna is converted to a voltage across a 1.2 nF on-chip storage capacitor (V_C) using six stages of self-driven voltage rectifier. A power management block is used after the harvesting unit to divide the operation of the system into two phases. The power Management Unit (PMU) is composed of a simple voltage comparator that monitors the voltage on the storage capacitor.

In order to minimize the power consumption of the PMU, all the transistors operate in deep sub-threshold region. In addition, we have used double-gate CMOS transistors to minimize the leakage current. V_C is divided using a chain of eleven diode-connected transistors before being fed to the comparator. The output node of the comparator (EN) acts as the input signal of the MUX, which changes the division ratio of V_C . The output node of the MUX is compared with a fixed reference voltage, which is used to form a hysteresis comparator. The reference generator operates based on the difference of threshold voltages of single-gate and double-gate CMOS transistors [35]. The reference generator provides different constant voltages for biasing the comparator. The resting phase of the system occurs when the EN signal is low. During this phase, the power harvesting unit charges the storage capacitor. Once V_C reaches to the high threshold level (V_H), the EN signal follows V_C , and consequently, the MUX decrease the division ratio. This serves as the beginning of the active phase of the system wherein the voltage regulator is connected to the storage capacitor.

At this phase, the stored electrical energy is drawn from the capacitor. As a result, V_C drops until it reaches the low threshold value (V_L). The maximum current that can be delivered to an external load by the voltage regulator is limited by the transient response of the comparator in the PMU. The reason is the time response of the comparator, is not fast enough to follow abrupt transitions of V_C . However, using

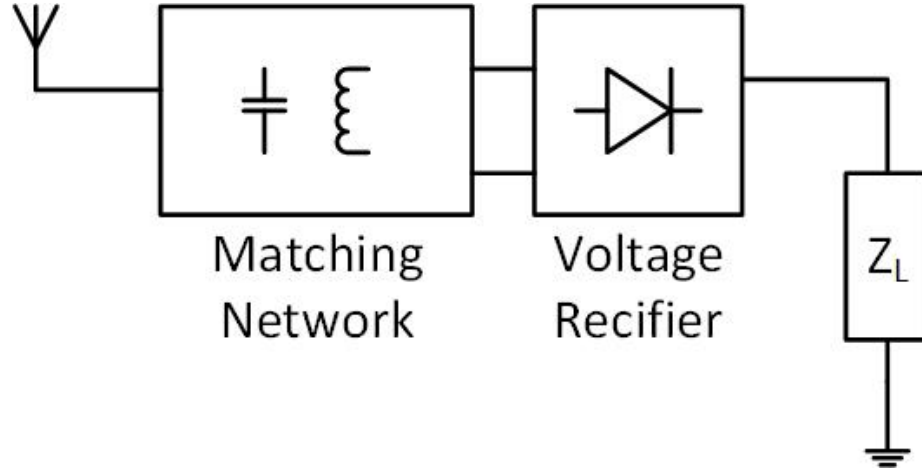


Figure 3.3: System architecture of a far-field wireless power harvester for ultra-low power implants.

larger storage capacitor can increase this transition time and mitigate the problem.

3.2 A Far-Field Power Harvesting Circuit for an Ultra-low Power Biomedical Implantable Device

The energy harvesting system is composed of an on-chip dipole antenna attached to a multi-stage voltage rectifier as shown in Figure 3.3. Area limitation dictates that the antenna maximum dimension must be as small as possible. A dipole antenna is selected as the receiver because it has a low profile structure and occupies a small area. It receives incident electromagnetic waves and passes them to the voltage rectifier in order to generate DC voltage at the output node of the rectifier. The considerations on rectifier design and the matching circuit are discussed in next chapters.

Wireless Link: Design and Characterization

4.1 Two-port Network Model

As stated in previous chapters, it is critical to transmit electromagnetic waves in a frequency that maximizes Power Transfer Efficiency (PTE). An analytic calculation in [28] reveals that a low-GHz frequency range is the optimum frequency for wireless power transmission into different biological tissues. Table 4.1 compares the optimum frequency for power transmission into different biological tissues with a thickness of 1cm. It is worth mentioning that these frequencies are calculated based on the assumption that the energy source is small and can be viewed as a magnetic or electric dipole. Solving Maxwell's equation and inserting medium Green's function results in calculating optimum frequency.

In [28], PTE is defined as the ratio of received power by the receiving antenna over absorbed power in biological tissue.

$$\eta = \frac{P_r}{P_{loss}} \quad (4.1)$$

Tissue Type	Approximate Optimum Frequency (GHz)
Cancellous Bone	3.80
Brain (Gray Matter)	3.85
Brain (White Matter)	4.23
Muscle	3.93
Skin (dry)	4.01

Table 4.1: Comparison of approximate optimum frequency for power transmission into 1cm of different biological tissues.

Optimum frequency is introduced as the frequency which maximizes the ratio in equation 4.1.

The optimum frequency with the definition of equation 4.1 is dependent on the type of tissue. In a practical case, a source cannot be approximated as a dipole. In addition, the impedance mismatch between the source and the transmitting antenna, and between the receiving antenna and the voltage rectifier affects optimum frequency. Impedance mismatch between the transmitting antenna and the source is not a serious issue since two impedances can be matched by exploiting the proper matching circuit. On the other hand, matching the load of the voltage rectifier to the impedance of the receiving antenna is a complex task, since any variation in tissue type or thickness changes the impedance of the receiving antenna. This thesis, therefore, considers the impedance mismatch of the receiving antenna in the optimum frequency calculation and defines the PTE as the ratio in equation 4.2.:

$$\eta = \frac{P_{delivered}}{P_{TX}}. \quad (4.2)$$

$P_{delivered}$ is the delivered power to a load connected to the receiving antenna, and P_{TX} is the input power to the transmitting antenna. This definition eliminates the effect of mismatch between the source and the transmitting antenna. However, once the optimum frequency is calculated based on this definition, the proper matching

component can be used to match the source to the transmitting antenna at the optimum frequency. In the remainder of this thesis, PTE refers to equation 4.2 unless stated otherwise.

Figure 4.1 shows power flow from an energy source on the transmitter side to a load connected to the receiving antenna.

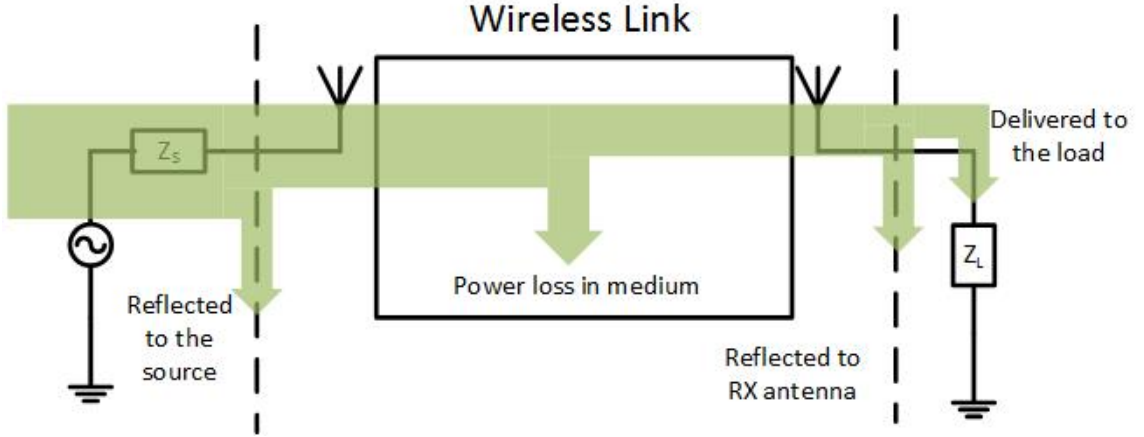


Figure 4.1: Power flow in a wireless power transfer system. The main reasons for power loss are impedance mismatch between the TX and RX antennas and their sources and thermal loss in the wireless link.

In order to optimize PTE, all the loss causes should be minimized. The energy transfer from the TX antenna to the receiving antenna can be formulated in several ways. Measuring scattering parameters is a general method for formulating energy transfer mechanism. It applies to all systems, regardless of their field region. The scattering parameter of a system is convertible to Z parameter or Y parameter and can be used to represent an equivalent circuit model for the configuration shown in Figure 4.1.

The wireless system in Figure 4.1 can be modeled with a two-port network that includes the wireless link TX and the RX antenna (Figure 4.2)

The S parameter matrix of the two-port network in Figure 4.2 is a 2×2 matrix

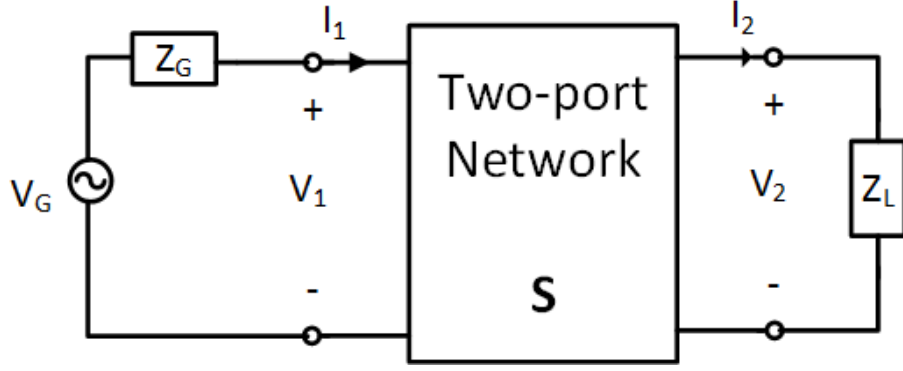


Figure 4.2: Two-port representation of the system shown in Figure 4.1.

that can be written as in 4.3,

$$S = \begin{bmatrix} s_{12} & s_{11} \\ s_{21} & s_{22} \end{bmatrix}. \quad (4.3)$$

Power reflection at different parts of the system shown in Figure 4.1 can be calculated using the following coefficients written in equations 4.4 – 4.7.

$$\Gamma_{in} = \frac{Z_{in} - Z_0}{Z_{in} + Z_0} = s_{11} + \frac{s_{12}s_{21}\Gamma_L}{1 - s_{22}\Gamma_L} \quad (4.4)$$

$$\Gamma_{out} = \frac{Z_{out} - Z_0}{Z_{out} + Z_0} = s_{22} + \frac{s_{12}s_{21}\Gamma_G}{1 - s_{11}\Gamma_G} \quad (4.5)$$

$$\Gamma_G = \frac{Z_G - Z_0}{Z_G + Z_0} \quad (4.6)$$

$$\Gamma_L = \frac{Z_L - Z_0}{Z_L + Z_0} \quad (4.7)$$

Z_0 is the reference impedance, which is $50 \, \Omega$ in this case. Γ_{in} and Γ_{out} are reflection coefficients at port 1 (input) and port 2 (output), respectively. Γ_{in} and Γ_G represent reflection coefficients at the load and the source, respectively.

Similar to [36], we use the \mathbf{S} matrix to calculate the system's power flow. The available power of the generator (P_{avG}) is the maximum power that can be delivered to the input port of the two-port network. In a case that network's input impedance (Z_{in}) is not conjugate matched to the impedance of the source (Z_G), a portion of P_{avG} reflects, and less power is delivered to the network (P_{in}).

An equivalent circuit model for the two-port network can be calculated by converting the \mathbf{S} matrix to a \mathbf{Z} matrix that includes impedance parameters of the two-port network. The \mathbf{Z} matrix can be calculated using the transformation in equation 4.8):

$$\mathbf{Z} = (\mathbf{I}_{2 \times 2} - \mathbf{S})^{-1}(\mathbf{I}_{2 \times 2} + \mathbf{S})^{-1} = \begin{bmatrix} Z_{11} & Z_{12} \\ Z_{21} & Z_{22} \end{bmatrix}. \quad (4.8)$$

In Figure 4.3, V_{Ind} is the induced voltage at the receiving side of the system due to the input power to the network. The values of V_{Ind} , Z_{in} , and Z_{out} are calculated in equations 4.9 – 4.11

$$V_{Ind} = \frac{Z_{21}V_G}{Z_{11} + Z_G} \quad (4.9)$$

$$Z_{in} = Z_{11} - \frac{Z_{12}Z_{21}}{Z_{22} + Z_L} \quad (4.10)$$

$$Z_{out} = Z_{22} - \frac{Z_{12}Z_{21}}{Z_{11} + Z_G} \quad (4.11)$$

P_{avG} , P_{in} , the maximum available power of the network at the output port (P_{avN}), and the delivered power to the load (P_L) are derived from the following

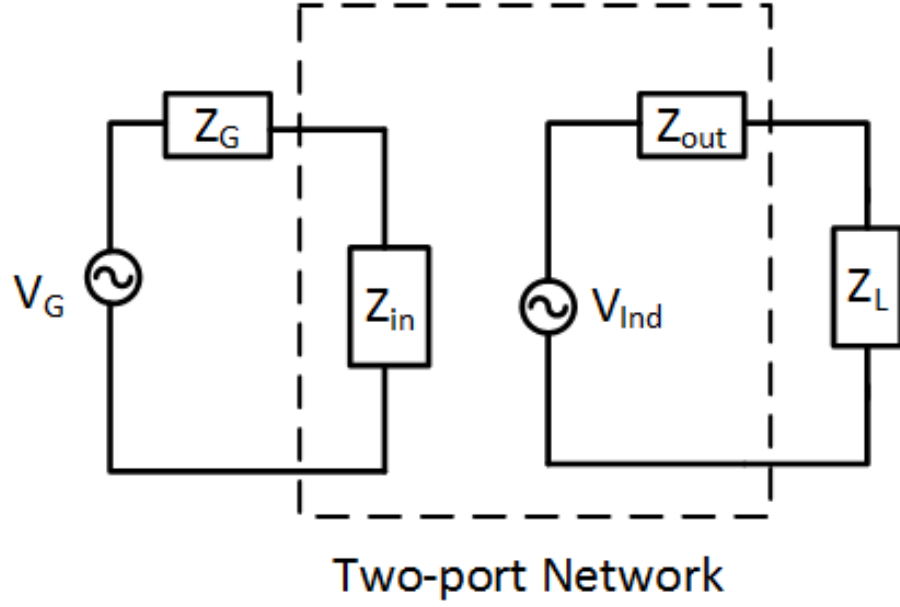


Figure 4.3: An equivalent circuit model for the two-port network in Figure 4.1.

equations which are calculated using the equivalent circuit model:

$$P_{avG} = \frac{|V_G|^2}{8Z_0} \frac{|1 - \Gamma_G|^2}{1 - |\Gamma_G|^2} \quad (4.12)$$

$$P_{in} = \frac{|V_G|^2}{8Z_0} \frac{(1 - |\Gamma_{in}|^2)|1 - \Gamma_G|^2}{|1 - \Gamma_{in}\Gamma_G|} \quad (4.13)$$

$$P_{avN} = \frac{|V_G|^2}{8Z_0} \frac{|1 - \Gamma_G|^2 |s_{21}|^2}{(1 - |\Gamma_{out}|^2)|1 - s_{11}\Gamma_G|^2} \quad (4.14)$$

$$P_L = \frac{|V_G|^2}{8Z_0} \frac{|1 - \Gamma_G|^2 |s_{21}|^2 (1 - |\Gamma_L|^2)}{|(1 - \Gamma_{in}\Gamma_G)(1 - s_{22}\Gamma_L)|^2}. \quad (4.15)$$

If the source is conjugate matched to the input impedance of the two-port network ($\Gamma_{in} = \Gamma_G^*$), P_{in} becomes equal to P_{avG} . Similarly, having a matching circuit at the output results in $\Gamma_{out} = \Gamma_L^*$ and maximizes the delivered power to the load.

4.2 Power Efficiency

We can use equations 4.12 – 4.15, to define different metrics for measuring power transfer efficiency in the diagram shown in Figure 4.1. Similar to [36], we define the fraction of delivered power to the load over available power of the source as transducer gain (G_T). Operating power gain (G_p) is another definition of power gain that is used frequently To calculate PTE in this chapter. As mentioned earlier in this thesis, PTE is calculated assuming the mismatch of the RX antenna and its load as an influential factor. It means that there is no matching circuit at the receiving side. In order to evaluate the effect of this mismatch on PTE, we introduce a new power gain: desired gain (G_{des}). G_{des} is the ratio of P_{avN} to P_{in} :

$$G_T = \frac{\text{Delivered power to load}}{\text{Maximum available power of generator}} = \frac{P_L}{P_{avG}} \quad (4.16)$$

$$G_p = \frac{\text{Delivered power to load}}{\text{Input power to network}} = \frac{P_L}{P_{in}} \quad (4.17)$$

$$G_{des} = \frac{\text{Maximum avaibale power out of network}}{\text{Input power to network}} = \frac{P_{avN}}{P_{in}} \quad (4.18)$$

The power gains in equations 4.16 – 4.18 can be expressed in terms of scattering parameters or impedance parameter. It is insightful to look to different power gains in a situation that Z_G and Z_L are matched to Z_0 . In this case, $\Gamma_G = \Gamma_L = 0$ and $\Gamma_{in} = s_{11}$, $\Gamma_{out} = s_{22}$. Recalculating power gains results in the reduced formats

written in equation 4.19:

$$G_T = |s_{12}|^2, G_p = \frac{|s_{21}|^2}{(1 - |s_{11}|^2)}, G_{des} = \frac{|s_{21}|^2}{(1 - |s_{11}|^2)(1 - |s_{22}|^2)}. \quad (4.19)$$

Equation 4.19 clearly shows the effect of mismatch on the PTE. In comparing the terms, it is evident that the portion of the generator's available power that is equal to $|s_{11}|^2 P_{avG}$ is reflected at the input port. Similarly, $|s_{22}|^2 P_{avN}$ is reflected at the output port of the network due to the mismatch. G_T is the most general term that includes the effect of impedance mismatches on both transmitting and receiving side. G_p only takes into account mismatches on the receiving side, while G_{des} is completely independent from any impedance mismatch and is a function of s_{21} . s_{21} can be views as a coupling coefficient that dominantly determines PTE when there is no impedance mismatch in the system. **S** matrix of a passive network is symmetric, which means that s_{12} and s_{21} are equal. This assumption is valid for all passive networks. In a passive network, $|s_{12}| \leq 1$. The equality only happens for a loss-less network and means that 100% of input power to the network is transferred to its output port. s_{12} is an intrinsic feature of the network that depends on the network's physical properties such as dimension and types of materials. A wireless link that includes material with high losses, has smaller s_{21} .

In a two-port network, the power loss due to impedance mismatch at the output port is usually reported by defining “input return loss” as seen in equation 4.20. “Insertion loss” and “output return loss” are two other terms used to formulate losses from the input port to the output and impedance mismatch at the output port (4.21, 4.22).

$$IRL = 10 \log_{10} \left| \frac{1}{s_{11}^2} \right| = -20 \log_{10} |s_{11}| (dB) \quad (4.20)$$

$$IL = -20\log_{10}|s_{12}|(dB) \quad (4.21)$$

$$ORL = 10\log_{10}\left|\frac{1}{s_{22}^2}\right| = -20\log_{10}|s_{22}|(dB) \quad (4.22)$$

The dependency of S parameters on the dimensions of the system implies that the impedance mismatch of TX and RX antennas is not the only factor that must be considered for designing an efficient power transfer method. Antenna structure and dimensions also could impact the S parameters and, consequently, change the performance of the system.

The losses in the wireless link are mainly caused by dielectric loss of biological tissue, which results in tissue heating and radiation and conduction losses in TX and RX antennas. However, tissue absorption dominates the losses in the antennas, thus, all losses can be attributed to biological tissues.

Before running numerical simulations on the system shown in Figure 4.1 and discussing design considerations of TX and RX antennas, the effect of biological tissues should be characterized and included in all simulations. In the rest of this chapter, we explain how to model dispersive behavior of biological tissues.

4.3 Multilayer Model of Tissue

Biological tissue has a dispersive behavior toward electromagnetic waves and absorbs power when exposed to EM radiation. The absorption increases in higher frequencies and causes tissue heating. In fact, different biological tissues behave like a lossy dielectric material with a frequency-dependent dielectric constant. The thickness and type of the constituent biological tissues in a wireless link impact the optimum frequency. Therefore, the frequency-dependent behavior, tissue composition,

and thicknesses should be determined before using numerical simulation to calculate the optimum frequency.

Because of the overwhelming use of cell phones and handheld devices, previous studies on tissue absorption focused primarily on human head tissue [37]. A multilayer model for heterogeneous tissue composition divides the constituent tissues into separate layers stacked on each other. This model considers a complex inhomogeneous composition as multiple planar layers and has been used and verified frequently [38, 39].

Figure 4.4 shows a multilayer model of human head. The thickness of constituent layers varies with age and sex, and from person to person. However, in a particular area of the head, the thickness of the layers is between two boundaries, as shown in Table 4.2. The data presented in this table were obtained from different people over the age of 10.

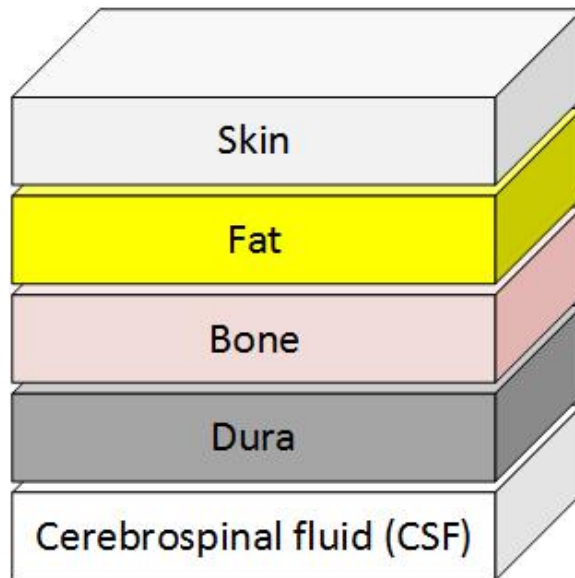


Figure 4.4: A multilayer model of a human head. Constituent tissues are modeled by multiple separated planar sheets.

the next step is to include frequency-dependent behavior of biological tissues.

Tissue Type	Thickness (mm)
Skin	1-2
Fat	1-2
Skull	1.5-7
Dura	1
CSF	0-2

Table 4.2: Thickness of constituent layers in human head multilayer model.

The complex permittivity of a biological tissue can be expressed as a real and an imaginary parts (equation 4.23). The imaginary part of a complex permittivity represents the losses due to charge bound and dipole relaxation phenomena, which cause energy loss, while the real part results in no losses.

$$\epsilon(\omega) = \epsilon_1(\omega) + i\epsilon_2(\omega) = \epsilon'(\omega) + i\frac{\sigma(\omega)}{\omega} \quad (4.23)$$

The complex permittivity of biological tissues can be calculated using a well-known Cole-Cole formula, which is a curve-fitting method for the measured complex permittivity values of different tissues [40]. As of now, I refer to the real part of the complex permittivity ($\epsilon_1(\omega)$) as “permittivity” and the imaginary part of the complex permittivity ($\epsilon_2(\omega)$) as “electric conductivity”.

Figures 4.5 and 4.6 show permittivity and conductivity of skin, fat, and bone tissue versus frequency respectively. As evident in Figure 4.5, permittivity of the tissues decreases in higher frequencies, which means that the tissues show less reactive behavior and store less energy. On the other hand, Figure 4.6 clearly shows that more energy loss is expected at higher frequencies since electrical conductivity of the tissues increases with frequency increments.

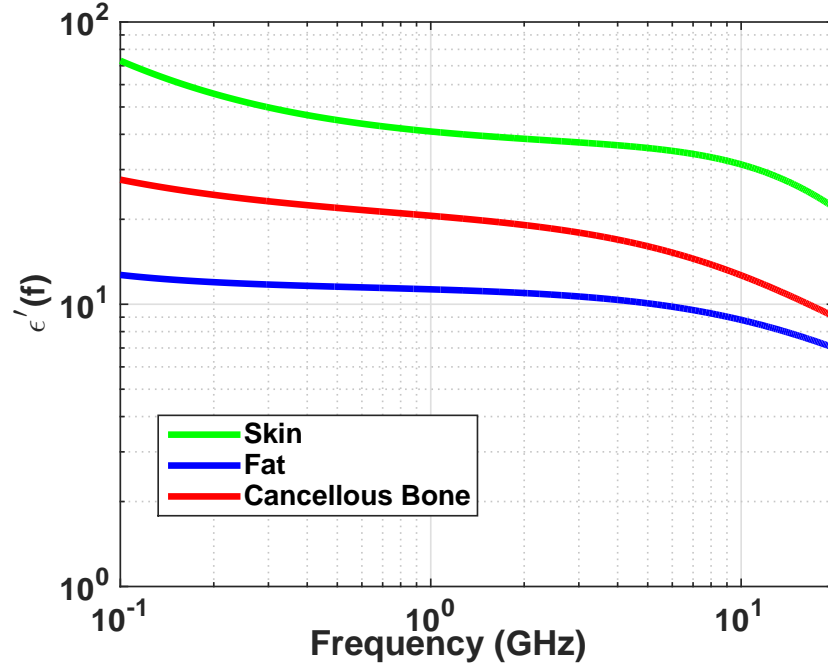


Figure 4.5: Electrical permittivity of skin, fat, and skull bone versus frequency.

4.4 Wireless Link Design

4.4.1 RX Antenna

Generally, integration of wireless implantable devices is hindered by RX antenna size. Most designs in past years exploited large coils to capture enough power for the operation implanted systems. In this thesis, one of the most important goals is to design a power harvesting system for mm-size implantable devices that can be integrated with a commercial CMOS technology.

As stated in chapter 4, the power harvesting systems in this thesis are designed with two different goals. Figure 3.2 shows the block diagram of the system for a high-performance biomedical implant such as a neural recording implant, and Figure 3.3 shows the block diagram of a far-field energy harvesting system designed for an ultra-low power implant.

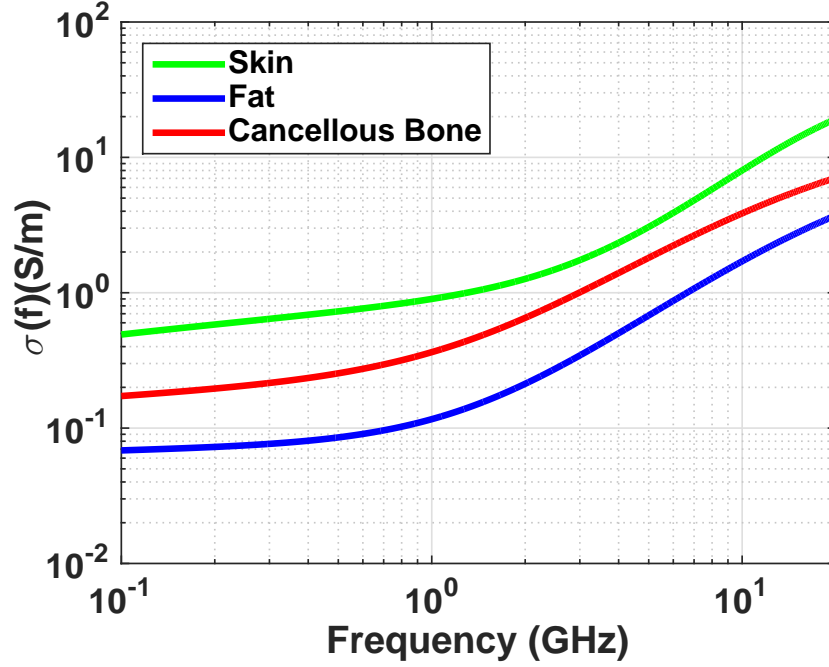


Figure 4.6: Electrical conductivity of skin, fat, and skull bone versus frequency.

The main goals of a far-field power harvesting system are to increase the operating distance and shrink the size of the chip. In order to fulfill both of these goals, an on-chip dipole antenna was chosen as the receiver because it has a low profile structure and occupies a small area. Area limitation dictates that the maximum antenna dimensions be as small as possible. The length of the antenna determines the maximum dimensions of the system; therefore, a 1.6-mm dipole antenna was exploited to capture electromagnetic waves. Since the goal is to operate the system in a far-field region with almost no coupling between transmitter and the receiver, the type of RX antenna is selected based only on area limitations. On the other hand, the mm-size power harvesting system for high-performance implants operate in a radiative near-field region, and the transmitting antenna is close to the implanted system and biological tissues. Similar to near-field wireless power transfer systems, a loop structure can work as a transmitter since its near-field electric field is small. Consequently, a loop antenna with two turns was selected as the RX antenna. Figure 4.7

demonstrates the structure and dimensions of the RX antenna used in the radiative near-field system. The load of this antenna is the voltage rectifier.

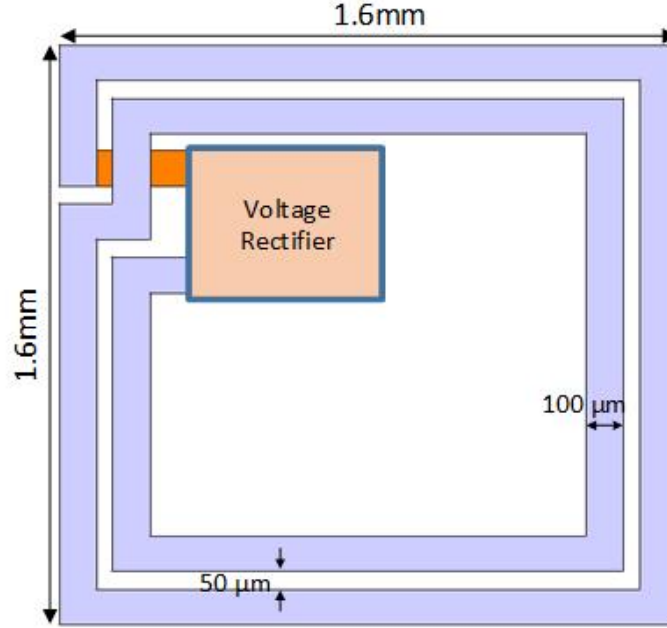


Figure 4.7: The loop antenna with two turns used in the design of the radiative power harvesting system.

Increasing the number of turns in the RX antenna increases the inductance of the coil. However, due to area limitation and the slight improvement of inductance results from more turns the RX antenna was designed with only two turns.

4.4.2 TX Antenna

4.4.2.1 Far-field Power Harvesting System

First, I discuss the considerations of TX antenna design for the far-field power harvesting system. In this case, the operating range of the system was determined by the sensitivity of the voltage rectifier and the input power to the TX antenna.

Since the system operates in a far-field region, the incident electromagnetic waves to the RX antenna are plane waves. In this case, the power transmission from the TX antenna to the RX antenna can be formulated with Friss transmission equation as seen in equation 4.24 [21, 41]:

$$\frac{P_r}{P_t} = G_t(\theta_t, \phi_t)G_r(\theta_r, \phi_r)\left(\frac{\lambda}{4\pi R}\right)^2(1 - |\Gamma_r|^2)(1 - |\Gamma_t|^2)e^{-2\alpha} \quad (4.24)$$

where G_t and G_r are the gain of the TX and RX antennas and Γ_t and Γ_r are the reflection coefficients between source/load and TX/RX antennas, respectively. The medium loss is accounted by the loss factor $e^{-2\alpha}$, where α is the absorption coefficient of the intervening medium.

According to the Friss transmission equation, the effects of the TX/RX antenna structure can be distinguished from those of the wireless link composition. Given a particular power budget on the transmitting side, using a TX antenna with higher gains delivers more power to the receiver. In the simulation, a dipole antenna was used as the TX antenna because it has the same polarization as the RX antenna and there would be no polarization loss.

4.4.2.2 Radiative Near-field Power Harvesting System

The power harvesting system in Figure 3.2 operates in a radiative near-field and there is a weak coupling between the TX and RX antennas. In addition, the plane wave assumption is not applicable to electromagnetic waves in this case. Unlike in a far-field system, the impact of antenna structure and the wireless link composition of s_{12} are not distinguishable. The dimensions and current distribution of the TX antenna considerably affect the S parameters of the system. In a near-field region, the magnetic field of a small-loop antenna is larger than its electric field. Therefore, a loop antenna was selected as the TX antenna to transmit power from the RF source.

Based on results of a numerical simulation, a $1\text{cm} \times 1\text{cm}$ loop antenna was selected as the transmitting antenna.

4.5 Power Harvesting System: Performance Evaluation

4.5.1 Far-field Power Harvesting System

Based on the multilayer model of a human head shown in Figure 4.4 and the considerations of TX and RX antenna design described in the last section, I use the following configuration to simulate a wireless power transfer system and calculate the PTE and the optimum frequency.

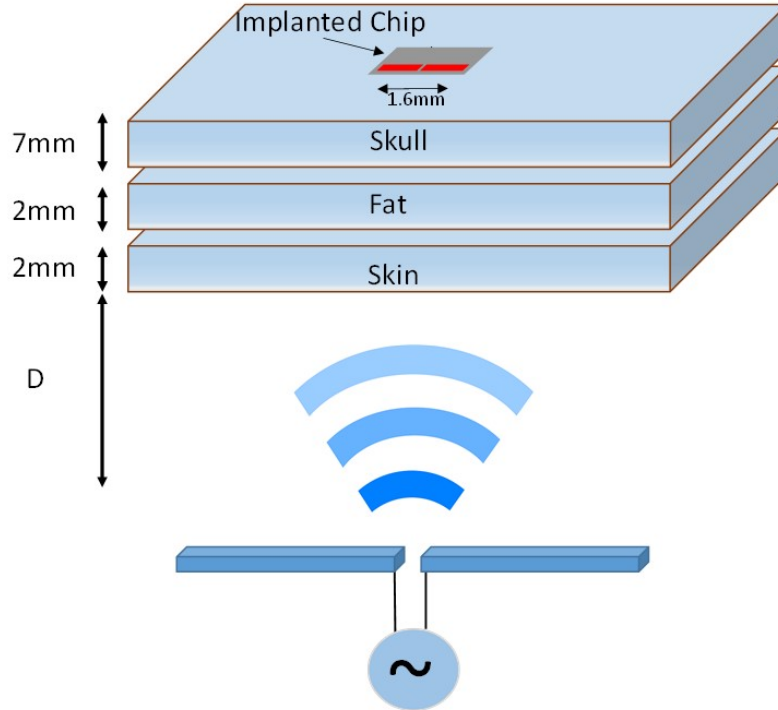


Figure 4.8: The simulation configuration of the far-field power harvesting system.

The desired power gain (G_{des}) of the system (shown in Figure 4.9) was calculated using the extracted simulated S parameters. that the maximum η can be achieved by setting the carrier frequency to 11.8 GHz. The maximum power transfer efficiency was calculated as -48dB. Using an array on the transmitter side can potentially increase the transmitter's gain, thus resulting in power transfer efficiency boosting. For instance, using a transmitter with a gain of 20 dB improves the power transfer efficiency to 28 dB, which is almost equal to the efficiency of the near-field coupling mechanism.

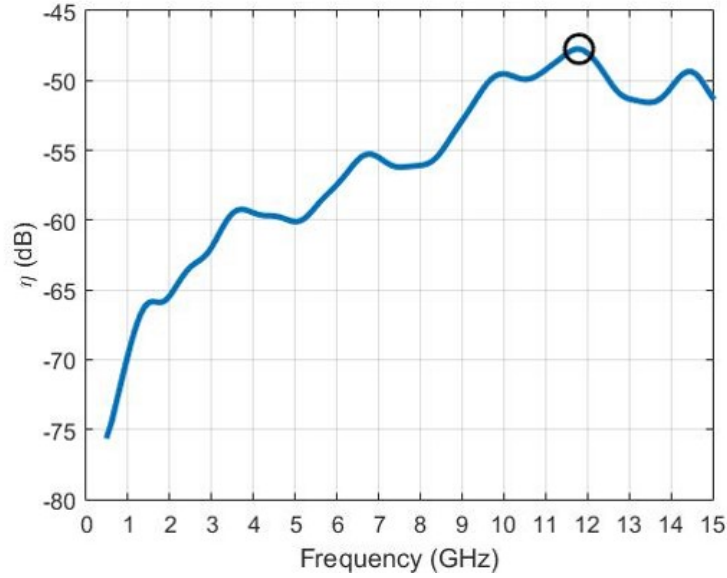


Figure 4.9: Power transfer efficiency versus frequency for the configuration depicted in Figure 4.8 with $D = 14\text{cm}$. The maximum efficiency is -48 dB at 11.8 GHz.

The simulation results was verified with the measurement setup shown in Figure 4.10. In this measurement, a broadband antenna is used as the transmitter while the chip is placed 15cm away and covered with a 1cm-thick layer of high-water content chicken breast. The chicken breast tissue was used to mimic the behavior of actual human head tissue, as its absorption coefficient is higher than skull and fat and is comparable to human skin tissue. Thus, in an actual case where the chip is

implanted in a human head, the losses caused by tissue absorption would be less than the power absorbed by the chicken breast. The power was generated by an E8257D PSG Keysight analog signal generator. The RX antenna was connected to an E4440A PSA series Keysight spectrum analyzer that shows the amount of received power at the transmission frequency.

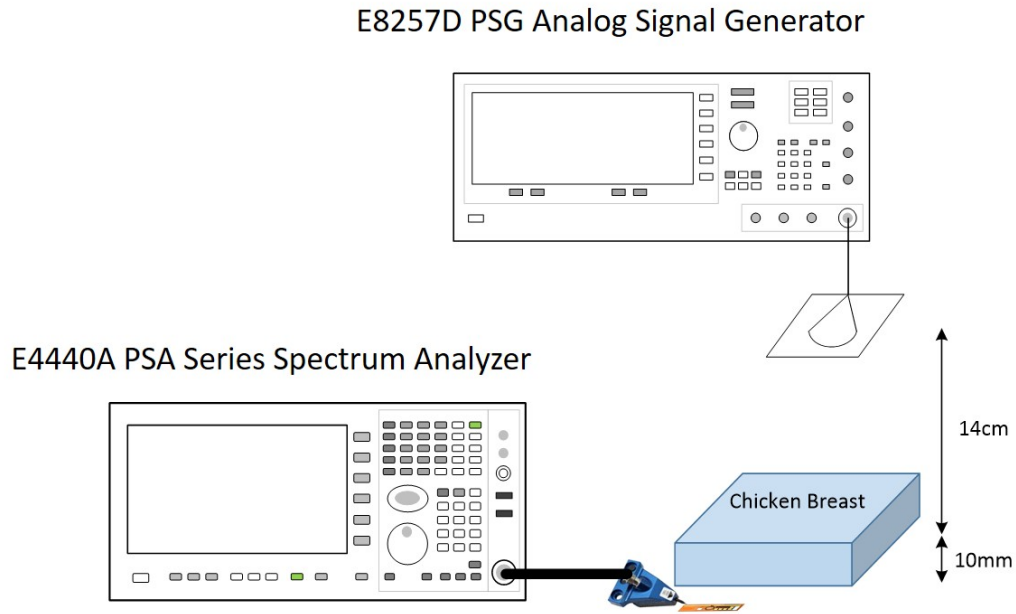


Figure 4.10: The measurement setup used for evaluating wireless link performance for the far-field power harvesting system.

It is worth mentioning that the signal generator and the spectrum analyzer have a $50\ \Omega$ impedance and that the mismatch of the TX and RX antennas was calculated and embedded from measurement results. The power transfer efficiency for multiple frequencies was measured and is plotted in Figure 4.11. Maximum efficiency was achieved at 11.2 GHz and measured as -51 dB. This result is close enough to the simulation results. The difference in the optimum frequency and the PTE can be explained by different types of biological tissue and different type of TX antennas

used in simulation and measurements.

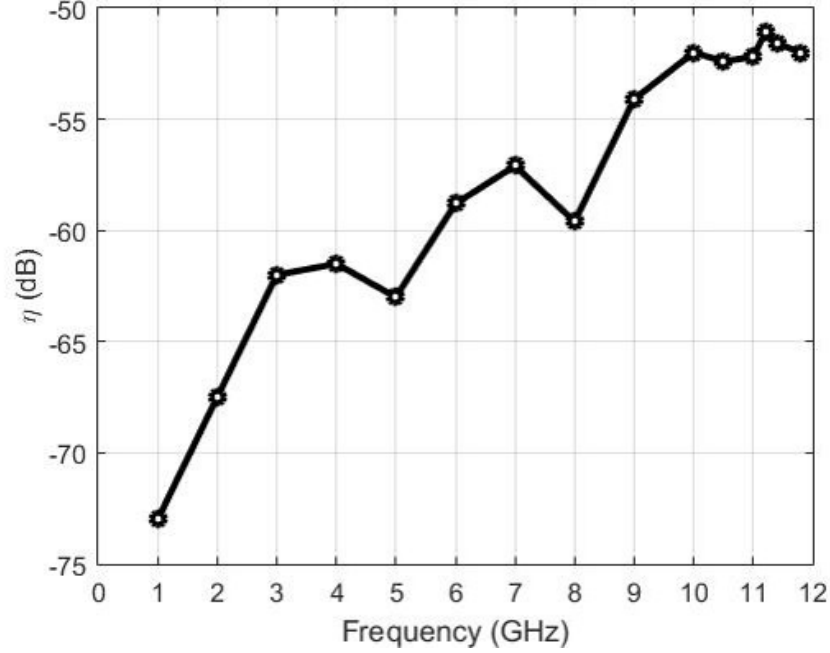


Figure 4.11: Measured power transfer efficiency versus frequency from a horn antenna with gain of 20 dB located 15cm above the energy harvesting system covered by 1cm of chicken breast. The maximum efficiency is -51 dB at 11.2 GHz.

4.5.2 Radiative Near-field Power Harvesting System

The PTE and the optimum frequency depend strongly on the wireless link composition and the dimensions of the antennas. As described previously, the dimensions of the RX antenna are determined by the area constraints imposed by the application requirement. The optimum dimensions of the TX antenna are determined through numerical simulation. Figure 4.12 shows the simulation configuration for the mm-size radiative near-field power harvesting system, including the intervening layers and antenna dimensions.

Simulation results show that for the radiative near-field system, the optimum frequency depends on both the TX antenna dimensions and the tissue composition

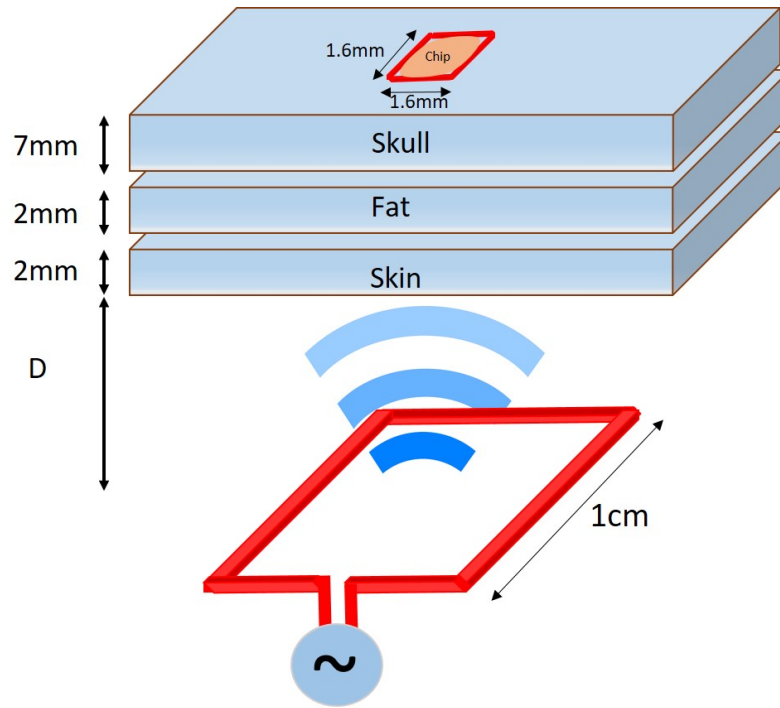


Figure 4.12: The configuration used to simulate the performance of the radiative near-field power harvesting system.

of the multilayer model, while the optimum frequency of a particular TX antenna is dominated by the tissue type and slightly changes with air-gap variation as long as the operating range is in the radiative near-field.

Figure 4.13 shows the measurement setup used to characterize the wireless link and measure the PTE. Similar to the far-field system measurement, a 1cm-thick chicken breast resembling high-water content biological tissue (such as human skin) was used to cover the power harvesting system, while a 1cm^2 loop antenna was connected to an Agilent N5230C network analyzer. The network analyzer provided the S parameter of the system that was used for PTE calculation. In addition, the impedance of the voltage rectifier, which is discussed in the next chapter, was measured by the network analyzer and the output return loss was calculated. The result

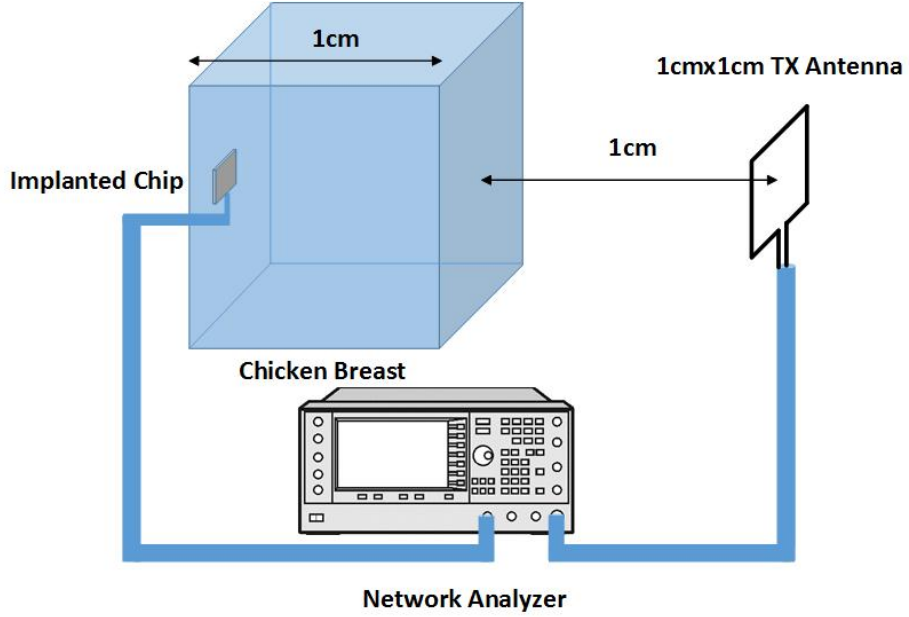


Figure 4.13: The measurement setup used to evaluate wireless link performance for the radiative near-field power harvesting system.

is depicted in Figure 4.14, where the PTE is plotted for conjugate matched load to the RX antenna and without matching. It clearly shows the effect of impedance mismatch on both the PTE and the optimum frequency. The best frequency for power transmission is 3 GHz when the RX antenna and the voltage rectifier are conjugate matched. In this case, the power harvesting system achieved a PTE of -21.8 dB. However, as evident in Figure 4.14 (bottom), the impedance mismatch on the receiving side attenuated the PTE by almost 7 dB and caused the optimum frequency shifts to 2.75 GHz, where the effect of impedance mismatch and link attenuation gave a PTE of -26.46 dB.

4.6 Specific Absorption Rate

Wireless power delivery to devices implanted in the human body is challenging because of the absorption of biological tissues and heating effect. The long-term

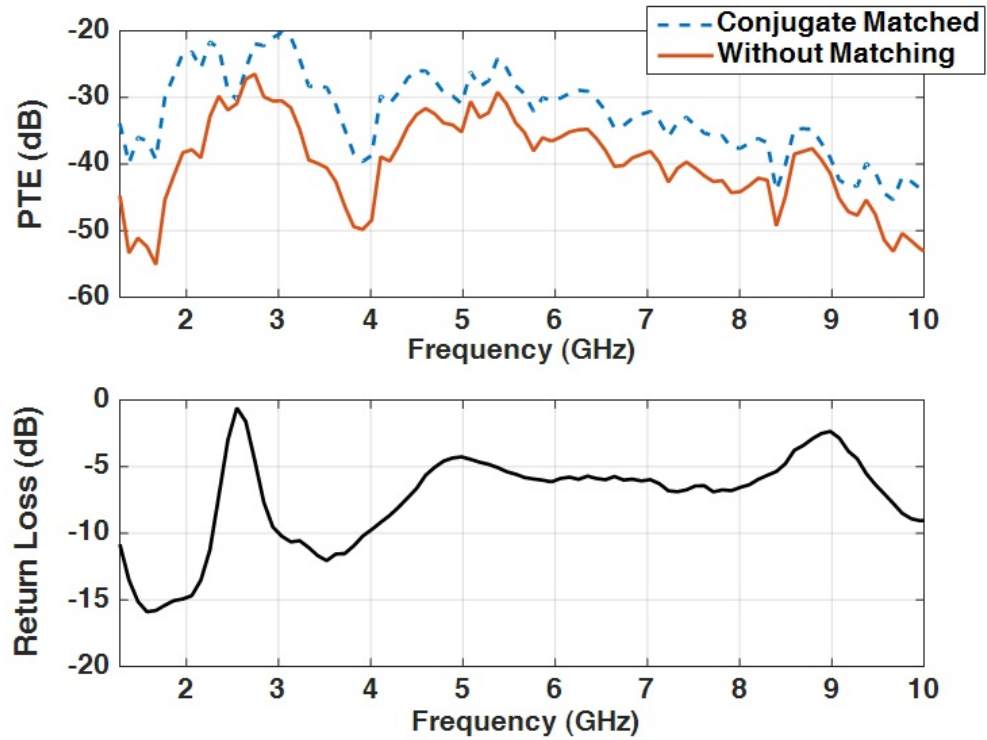


Figure 4.14: (top) The PTE of the radiative near-field system for a conjugate matched load and without any matching circuit connected to a voltage rectifier; (bottom) the return loss at the output port of the two-port network.

exposure to RF and microwave waves has proven very dangerous and has raised serious concerns regarding the effects of electromagnetic waves on the human body. Specific Absorption Rate (SAR), defined as the absorbed power per unit of mass in a particular type of biological tissue, is a well-known parameter for quantifying energy absorption by biological tissue. Safety regulations and limits have been proposed by different organizations and nationalities [19]. The IEEE safety standard for human exposure to electromagnetic fields in the RF and microwave frequency range of 3 KHz to 300 GHz is IEEE Standard C95.1-2005. The allowable absorption is specified as 10W/kg for the whole body and 0.4W/kg for local SAR. The European Union limits the SAR exposure to 2 W/kg, and the SAR limit set by the FCC is 1.6W/kg. SAR can be calculated according to equation 4.25, where σ is the electrical conductivity

of the tissue (S/m) and ρ is the density of the tissue (Kg/m^3):

$$SAR = \frac{\sigma}{2\rho} |\bar{E}|^2 \text{ (W/Kg)} \quad (4.25)$$

In order to figure out how much power can be delivered to a mm-size power harvesting system operating in a radiative near-field, the configuration shown in Figure 4.12, $D = 1\text{cm}$, is simulated with CST Microwave CAD tool. The maximum SAR value is calculated using IEEE C95.3 averaging method averaged over 10 gram of tissue and is plotted in Figure 4.15 at multiple frequencies.

The maximum deliverable power to the system cannot be increased more than a few hundred microwatts. Based on the Figure 4.15c, at the optimum frequency, the maximum deliverable power to the system is $383 \mu\text{W}$ when the SAR is less than 1.6 W/kg . The next chapter describes a power management technique that enables the system to deliver milliwatts of power to a high-performance implanted device.

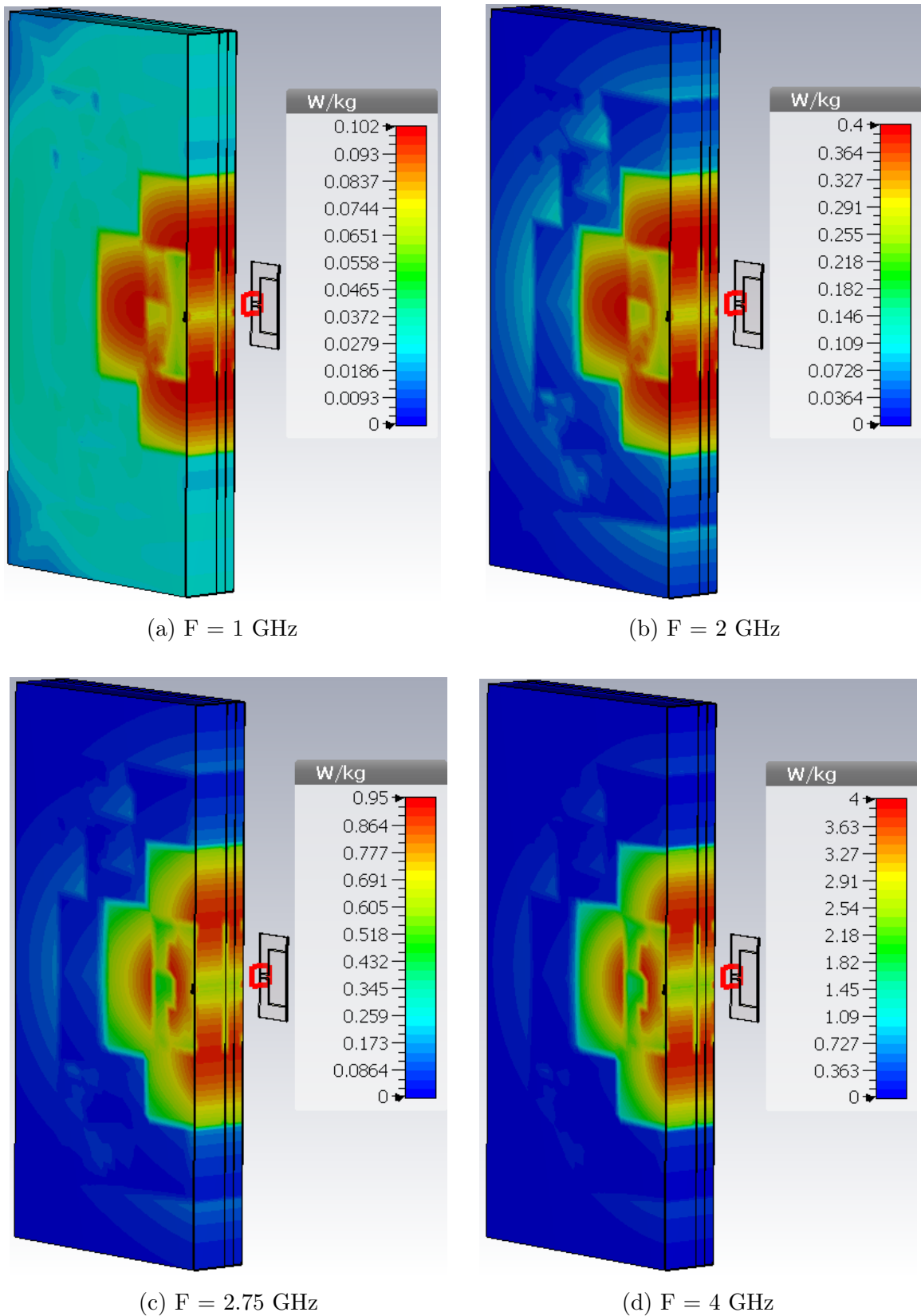


Figure 4.15: Specific Absorption Rate in intervening biological tissues in human head at different frequencies. The reference power: 1W transmitted from the TX antenna.

Design of the Wireless Power Harvesting System

Circuitry

5.1 Far-field Power Harvesting System

The system architecture of the far-field power harvesting system is described in chapter 4, Figure 3.3. The main goals of this design are increasing operating range for an ultra-low power load and a small area are discussed in chapter 6. Except for PTE and impedance mismatch between the RX antenna and the voltage rectifier, the sensitivity of the voltage rectifier is another important design metric that greatly affects the system's operating range. In the rest of this section, first, the design process of the voltage rectifier and the requirements are described. Then, a matching network is introduced for matching RX antenna to the voltage rectifier.

5.1.1 Voltage Rectifier

Depending on the incident RF signal amplitude, different structures can be used to implement the voltage rectifier. Usually, structures with higher efficiencies require high voltage amplitudes to be activated and are less sensitive. Considering the SAR

limitation, the radiated power cannot be increased arbitrarily. Moreover, because of the wireless link attenuation, the maximum available power at the rectifier's input port is limited. The voltage rectifier used in this work is based on a Dickson structure, which uses diode-connected CMOS transistors. Figure 5.1 demonstrates the schematic of a multi-stage Dickson voltage rectifier. It is composed of multiple diode-connected NMOS transistor.

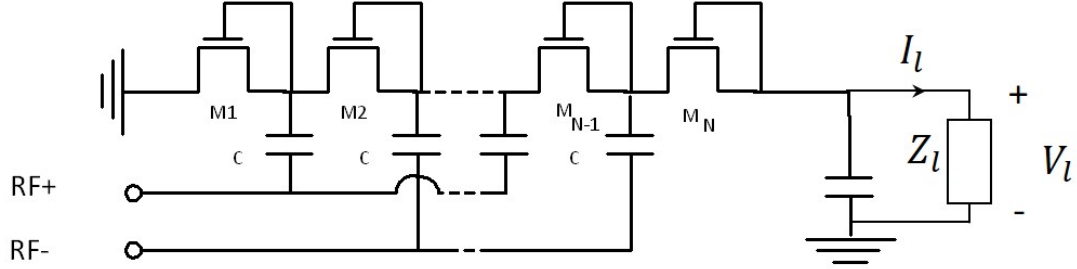


Figure 5.1: The schematic of a multi-stage Dickson voltage rectifier.

The rectifier's nominal load is 1A at 1V, and a single stage rectifier unit is unable to provide the required voltage since the RF signal has low amplitude. The output voltage level can be increased by cascading multiple stages of rectifier units. The conversion efficiency and sensitivity of these rectifiers depend mainly on the threshold voltage of the CMOS transistors; the voltage at the output node is calculated according to equation 5.1, where C is the coupling capacitor used to insulate DC voltages of internal nodes from incoming signals picked by the antenna [42]:

$$V_l = N \left(\frac{C}{C + C_p} V_{RF} - \frac{I_l}{f(C + C_p)} - V_{th} \right) - V_{th} \quad (5.1)$$

C_p is the parasitic capacitance at each charging pump, and V_l , I_l are the load voltage and current, respectively. V_{th} represents the threshold voltage of the transistors. As is evident from equation 5.1, for a given load, the number of transistors and the threshold voltage of the exploited device dominantly control the output voltage.

Decreasing the threshold voltage of the CMOS transistor leads to sensitivity and efficiency improvement. A simple method for decreasing the threshold voltage of the transistors is to place a DC voltage source between the gate and the source of each transistor, as depicted in Figure 5.2.

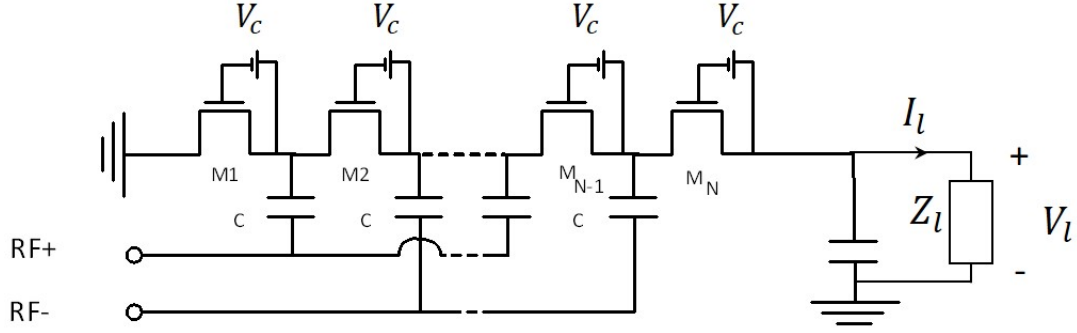


Figure 5.2: A threshold voltage reduction example by placing an external DC source between the gate and source terminals of each transistor.

Reducing the threshold voltage by placing an external DC source is not feasible for energy harvesting circuits. Therefore, another technique threshold compensation was used to reduce the threshold voltages.. The output voltage of each rectifier stage in Figure 5.1 is greater than the output of previous stages. In a multi-stage rectifier structure, the required voltage for overcoming the threshold voltage of CMOS transistors can be reduced by connecting their gate to the output of the next stage. This is the threshold compensation technique. Threshold compensation order is defined as the number of transistors in a closed loop that includes the connecting path from the gate of a transistor to the output node of another stage. The order of compensation is dependent on the output voltage requirement and the process threshold voltage [42]. We used 10 stages of rectifying unit with a threshold compensation order of 4. The 10-stage voltage rectifier with threshold compensation of order 4 is shown in Figure 5.3

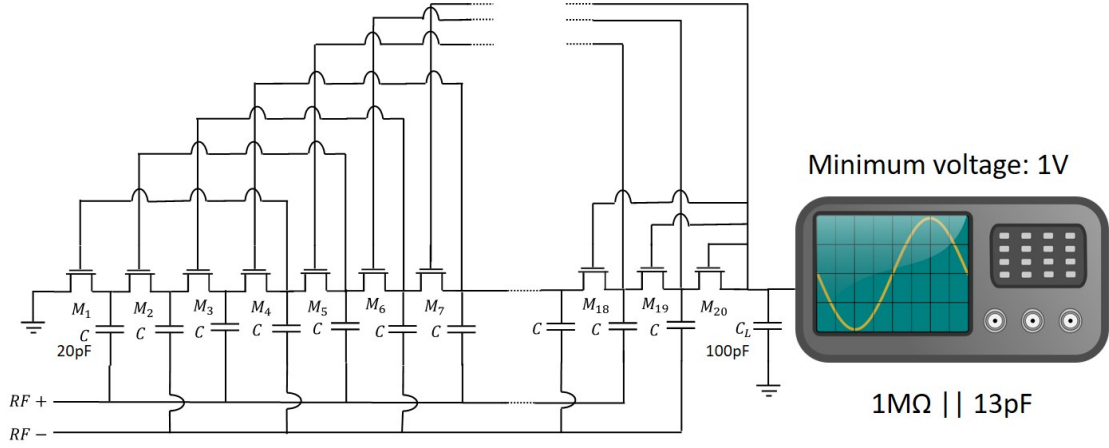


Figure 5.3: The schematic of a multi-stage Dickson voltage rectifier with a threshold compensation order of 4 connected to a voltage oscilloscope with an input impedance of $1\text{ M}\Omega$ parallel to a 13 pF capacitor.

5.1.2 Matching Network

Mismatch between the dipole antenna and the voltage rectifier is another important source of power loss in energy harvesting systems. It can greatly affect the sensitivity and efficiency of the system; therefore, a matching network was designed to match the output impedance of the antenna to the input impedance of the rectifier.

The input impedance of the multi-stage rectifier can be modeled as a parallel RC network. On the other hand, at the operating frequency, the wavelength is larger than 10 times the dipole antenna length ($\lambda \geq 10 \times l$). Therefore, dipole antenna output impedance at the carrier frequency consists of a capacitive part and a real part and can be calculated based on the simulation results. With the values of these two impedances known, a matching circuit was implemented, as shown in Figure 5.4, to maximize the voltage across rectifier's input ports.

The shunt inductor (L_M) was designed to resonate with the dipole antenna and voltage rectifier and to maximize the amplitude of the RF signal.

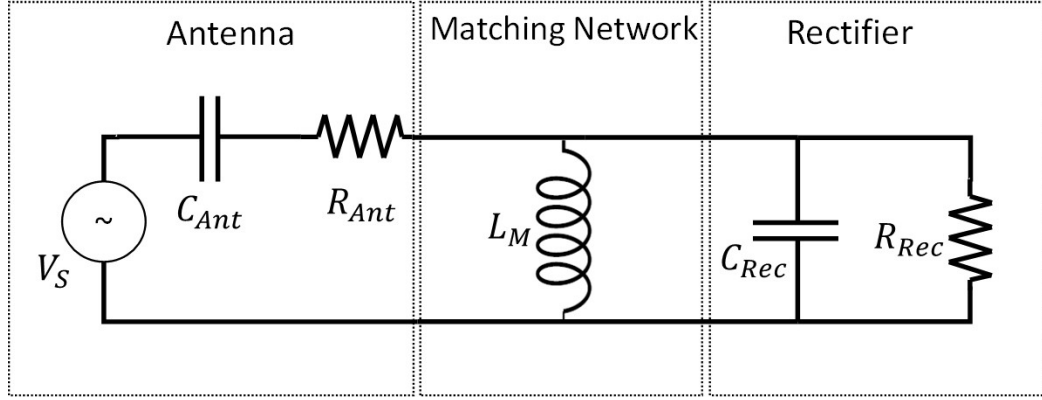


Figure 5.4: The schematic of the matching network. The inductance L_M resonates out with the the input capacitance of the rectifier.

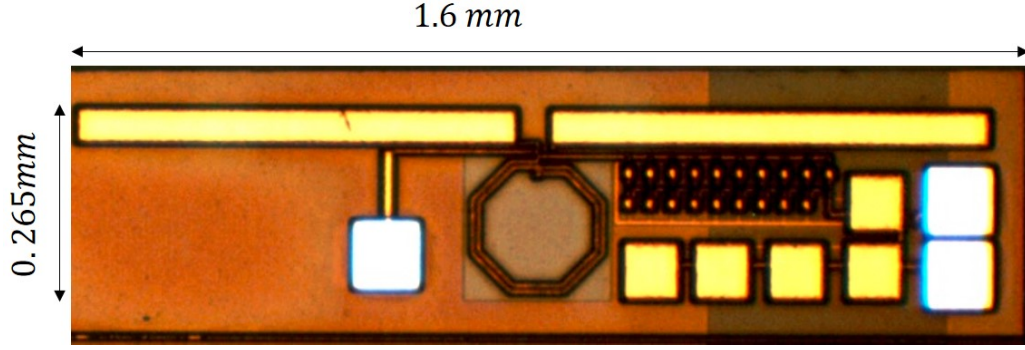


Figure 5.5: The chip micrograph of the far-field power harvesting system. The chip was fabricated in a 180nm SOI CMOS technology with a total area of 0.42 mm^2 .

5.1.3 Measurement Result

This design was fabricated in 180 nm SOI CMOS technology, and the chip was tested to verify the simulation results. The chip micrograph is shown in Figure 5.5. The total area of the chip, including a dipole antenna, matching circuit and multi-stage rectifier, was 0.42 mm^2 [43].

The measurement setup is represented in Figure 5.6. At the operating frequency (11.2 GHz), a horn antenna was used to increase the EIRP power. Radiating 2W from a horn antenna with a gain of 10 dB provided an AC signal at the rectifier input port, which is increased to 1V after rectification. An on-chip capacitor was connected

E8257D PSG Analog Signal Generator

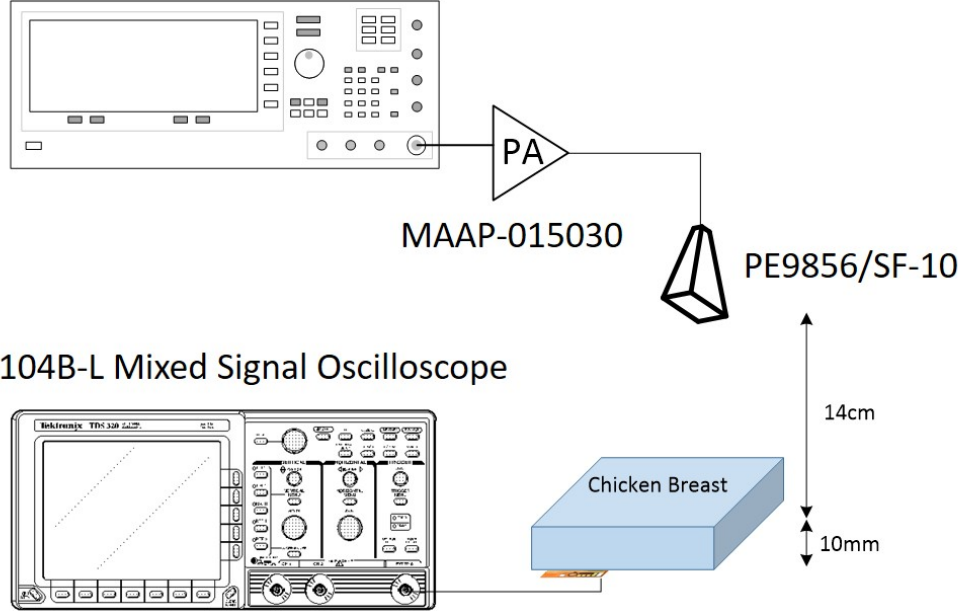


Figure 5.6: The measurement setup used for evaluating the performance of the fabricated power harvesting system shown in Figure 5.5. The mixed signal oscilloscope acts as the load of harvesting system, $1\text{ M}\Omega \parallel 13\text{ pF}$.

to the output of the voltage rectifier to absorb the voltage fluctuation, and a $1\text{ M}\Omega$ load, which is the input impedance of the oscilloscope, was connected to the output node of the rectifier as a nominal load. The minimum required power for achieving 1V with a $1\text{ M}\Omega$ load was measured as $23\text{ }\mu\text{W}$ (-16.3 dBm). The measured values for the input impedance of the voltage rectifier at 11.2 GHz were $Z_{rec} = 3.23 - 46.81j$, which is equivalent to a parallel $681\text{ }\Omega$ resistor and 0.338 pF capacitor. The dipole antenna output impedance at the same frequency is calculated as $Z_{ant} = 5.49 - 89.1j$. Based on these impedances, a 0.577 nH inductor is placed between the antenna and rectifier, as in Figure 5.4.

Finally, the output voltage of the rectifier is measured for different transmitted power levels and is plotted in Figure 5.7. It is evident that for a power level below

0.4W, the power at the input terminals of the rectifier is not enough to overcome the threshold voltage of the transistors, and thus the voltage rectifier is not activated. It is also worth noting that the voltage increment versus transmitted power level is not linear and that curve saturates for power levels higher than 2W. The reason is that increasing the voltage level at the internal nodes of the voltage rectifier in Figure 5.3 causes threshold reduction; if the threshold voltage of the transistors reaches to value near zero, they will conduct current in both directions and will not act like a diode. Hence, the efficiency of the rectifier will degrade.

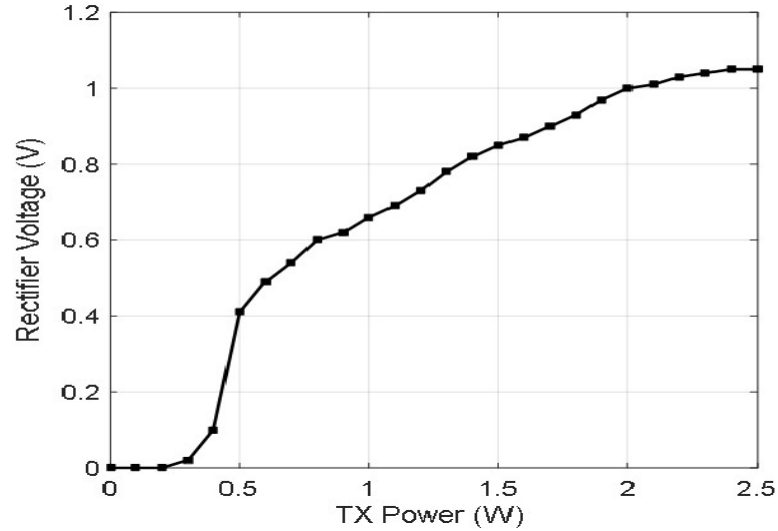


Figure 5.7: The output voltage of the far-field power harvesting system versus transmitted power level.

5.2 Radiative Near-field Power Harvesting System

The architecture of this system is described in chapter 4, and the constituent analog subsystems are briefly introduced in chapter 3. The maximum amount of deliverable power to the implanted system for a mm-size power harvesting platform cannot be increased more than a few hundred microwatts without violating safety

limits. Therefore, the system operation is divided into two different phases to enable the power harvesting system to deliver enough power to a high-performance biomedical implant such as a neural recording system. The power management unit (PMU) is composed of a scavenging unit and mode-changing unit, as shown in Figure 5.8

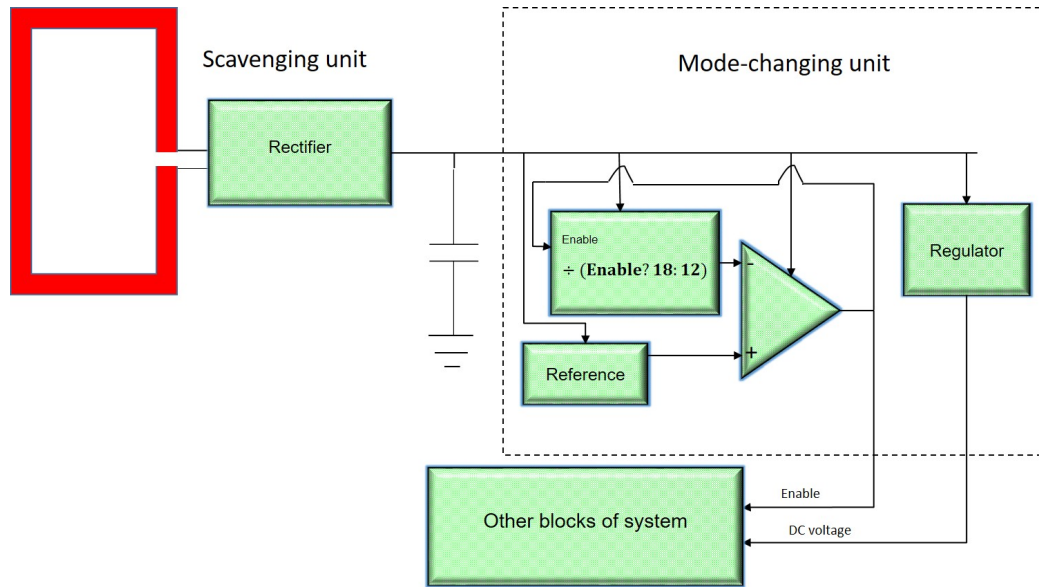


Figure 5.8: The block diagram of PMU. The PMU is composed of scavenging and mode-changing units.

The antenna design is described in the last chapter. This section describes the design details of each constituent block shown in Figure 5.8.

5.2.1 Voltage Rectifier

For the power harvesting system not operating in a far-field region, the amplitude of the incident electromagnetic waves is sufficient to overcome the threshold voltages of CMOS transistors. The topology of the best rectifier for a particular application mainly depends on the open voltage RF amplitudes. In most cases, the amplitude of the RF incident waves is not enough to reach the desired DC voltage level at the output. In this case, using multiple cascaded stages of rectifiers increases

the voltage level at the output node. The number of stages should be selected carefully, since more stages results in more losses and a drop in efficiency. The overall conversion efficiency is strongly dependent on the efficiency of a single rectifier unit and the number of stages. The rectifier typologies with higher conversion efficiency require more power for activation. Compared to other rectifier typologies, self-driven voltage rectifiers provide a good balance between efficiency and minimum power for activation [44]. In this design, I used six stages of self-driven voltage rectifier as is depicted in Figure 5.9.

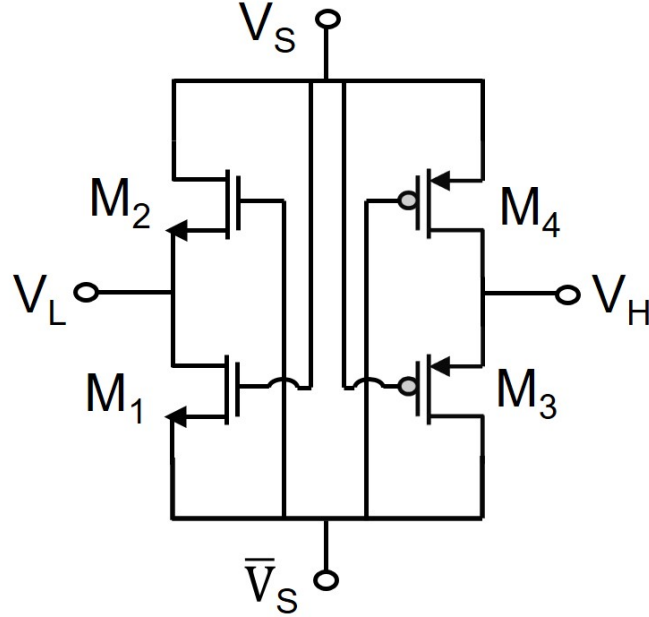


Figure 5.9: The schematic of a self-driven voltage rectifier.

V_S and \bar{V}_S represent the terminals of the RX loop antenna. The basic principle for the operation of the voltage rectifier is based on varying impedances of the transistors in different cycles of sinusoidal signals picked up by the antenna. Each transistor has shows a resistance toward AC currents that follow different branches in the circuit shown in Figure 5.9. In the positive cycle when $V_S \geq 0$ and $\bar{V}_S \leq 0$, the gate-source voltage of transistors M_1 and M_4 moves in a way that reduces the

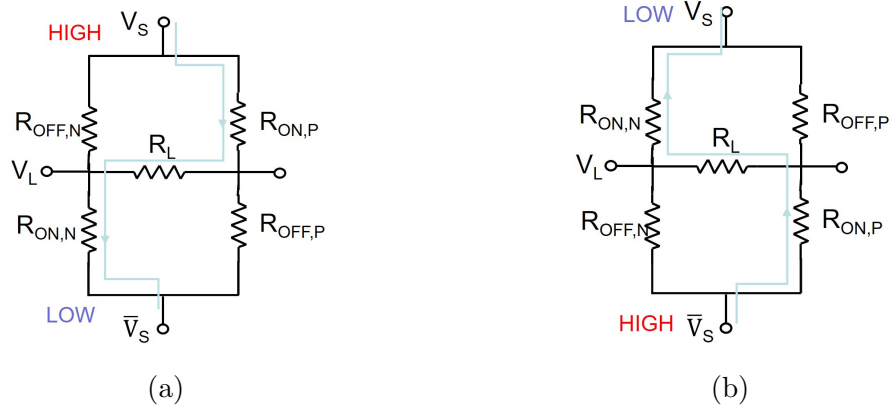


Figure 5.10: The equivalent circuit of the voltage rectifier during positive and negative cycles of the incident sinusoidal waves.

resistance of these devices. At the same time, M_2 and M_3 experience a gate-source voltage that causes their resistance to increase. The rectifier circuit can be modeled by the following circuit, shown in Figure 5.10, where R_L represents the equivalent resistance between input and output nodes of the rectifier (V_L and V_H).

Current flow is demonstrated in Figure 5.10. As is evident in this figure, the direction of the current in R_L is maintained in the same direction during positive and negative cycles. This means the establishment of a signal across input and output nodes of the rectifier that has a DC mean value. Putting a capacitor at the output node results in a fixed DC voltage that can be used to power internal circuits.

The input impedance of the voltage rectifier can be modeled by a parallel RC network. The parallel resistance includes parasitic resistances and the delivered power to the load. The parallel capacitance (C) also includes linear and nonlinear components. As a result, both R and C values are dependent on the load and the input level signal [45]. Because of the two-phase operation of the system, the load of the voltage rectifier changes from phase to phase. However, the power delivery is done in the resting phase when the only active part of the system is the mode-changing unit, as shown in Figure 5.8. The mode-changing unit is designed to consume a very negligible current;

therefore, the load of the voltage rectifier is almost constant. The input impedance of the voltage rectifier is measured using the network analyzer with an input power level of -6 dBm. The real and imaginary parts of the input impedance of the six-stage voltage rectifier are plotted in Figure 5.11.

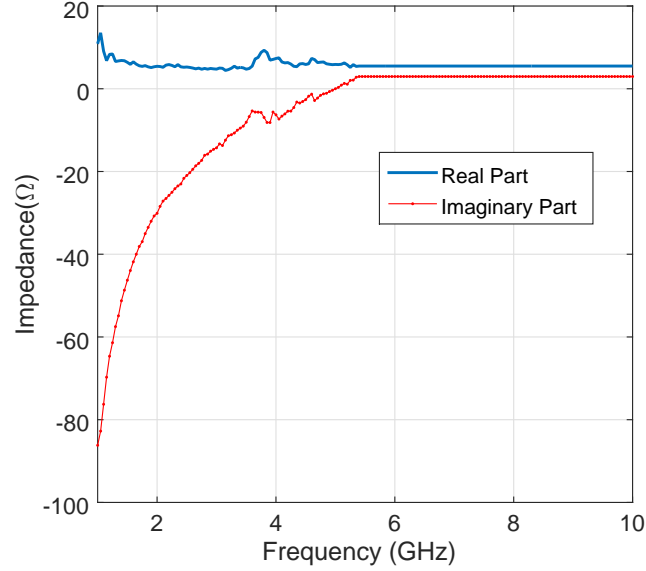


Figure 5.11: The real and imaginary parts of the input impedance of the designed six-stage voltage rectifier versus frequency with the input power level of -6 dBm.

Although conjugate matching between the voltage rectifier and the antenna improves the efficiency of the link by several dBs, it needs an external controller in order to adaptively match the impedances [46]. Therefore, mismatches between the RX antenna and the voltage rectifier are included in optimum frequency calculations.

5.2.2 Mode-changing Unit

The detailed block diagram of the mode-changing unit is shown in Figure 5.12. This unit is active in both the resting and active phases of the system. Therefore, the power consumption of this block should be minimized as much as possible in order to increase the power conversion efficiency and operating range and to reduce the

charging time of the storage capacitor.

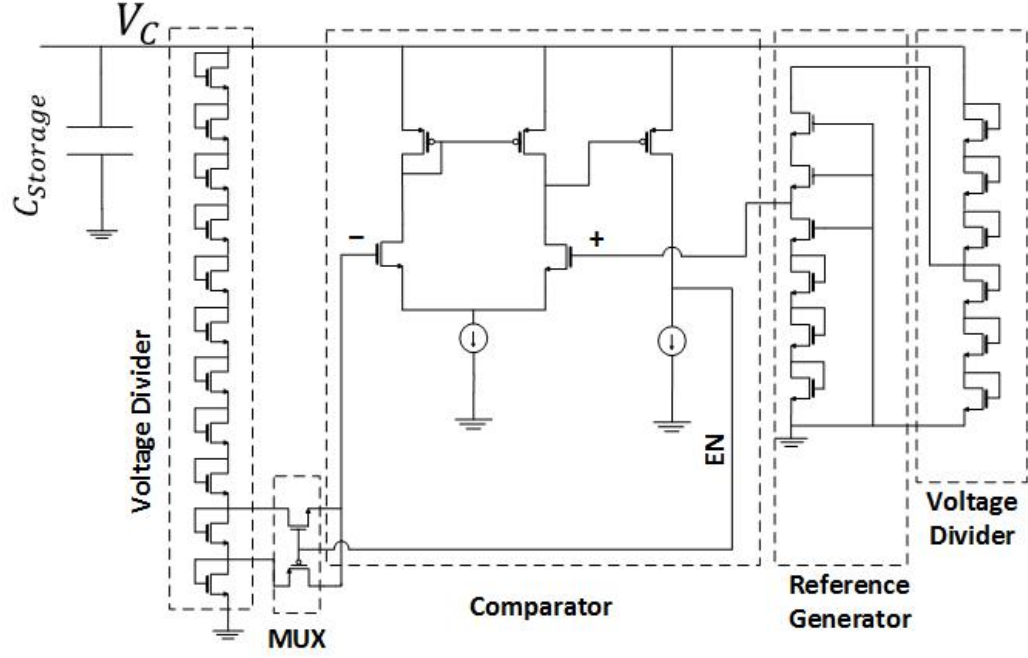


Figure 5.12: The circuit schematic of the mode-changing unit, which includes a voltage comparator, a reference voltage generator, and MUX for changing the division ratio.

All transistors in the mode-changing unit are pushed to work in a deep sub-threshold region where the drain current of each transistor can be calculated according to equation 5.2:

$$I_{sub} = \mu C_{ox} \frac{W}{L} (m-1)^2 V_T^2 \exp\left(\frac{V_{gs} - V_{th}}{m V_T}\right) \left(1 - \exp\left(\frac{-V_{ds}}{V_T}\right)\right). \quad (5.2)$$

Equation 5.2 is only valid for gate-source current less than the threshold of the transistor ($V_{gs} \geq V_{th}$) and positive drain-source voltages ($V_{ds} \geq 0$). In this equation, $m = 1 + \frac{C_d}{C_{ox}}$, $\mu = \text{carrier mobility}$, $V_T = \frac{kT}{q}$.

The time response of the system during discharging is limited by the voltage comparator. An obvious solution to improve the slew-rate of the system is to dissipate

more power and increase the current consumption, which degrades the sensitivity of the power harvesting system. An alternative approach is to deliver the same amount of power during the discharging phase and maintain the same discharging time. Increasing the size of the storage capacitor can lead to discharging time reduction and can be used to limit the discharge time to the maximum slew rate of the comparator. The voltage reference provides a constant DC voltage for the comparator to be compared to the MUX output. The principle underlies the operation of the reference voltage reference and can be comprehended by calculating the drain currents of M_1 and M_2 in Figure 5.13. Equating the drain currents of the transistors that operate in the deep sub-threshold region and finding the V_{ref} results in the following equation:

$$V_{ref} = \frac{m_1 m_2}{m_1 + m_2} (V_{th2} - V_{th1}) + \frac{m_1 m_2}{m_1 + m_2} V_T \ln \left(\frac{\mu_1 C_{ox1} W_1 L_2}{\mu_2 C_{ox2} W_2 L_1} \right) \quad (5.3)$$

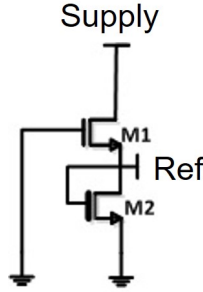


Figure 5.13: The schematic of an ultra-low power reference voltage generator circuit. Both transistors are working in the sub-threshold region.

Based on equation 5.3, the two transistors in the reference generator circuit should have different thresholds to avoid varying aspect ratios. For these reasons, we used a single-gate NFET as M_1 and a double-gate NFET as M_2 . Double-gate NFETs have greater threshold voltage than single gate NFETs. By setting a proper dimension for the transistors and stacking them as shown in Figure 5.8, higher reference values can be achieved based on a similar operation principle.

5.2.3 Voltage Regulator

During the discharging phase, the PMU enables all blocks of the system. The accumulated charge over the storage capacitor is drawn quickly. The blocks in the active mode require a constant DC for the operation, which is not affected by large voltage fluctuation over the storage capacitor. The voltage regulator is designed to deliver a constant DC voltage to the building blocks of the system during discharging time. The circuit schematic of the voltage regulator is shown in Figure 5.14. Since the voltage regulator operates in the active phase of the system, the power budget concern has been relaxed in the design. The reference voltages are generated by the structure shown in Figure 5.14.

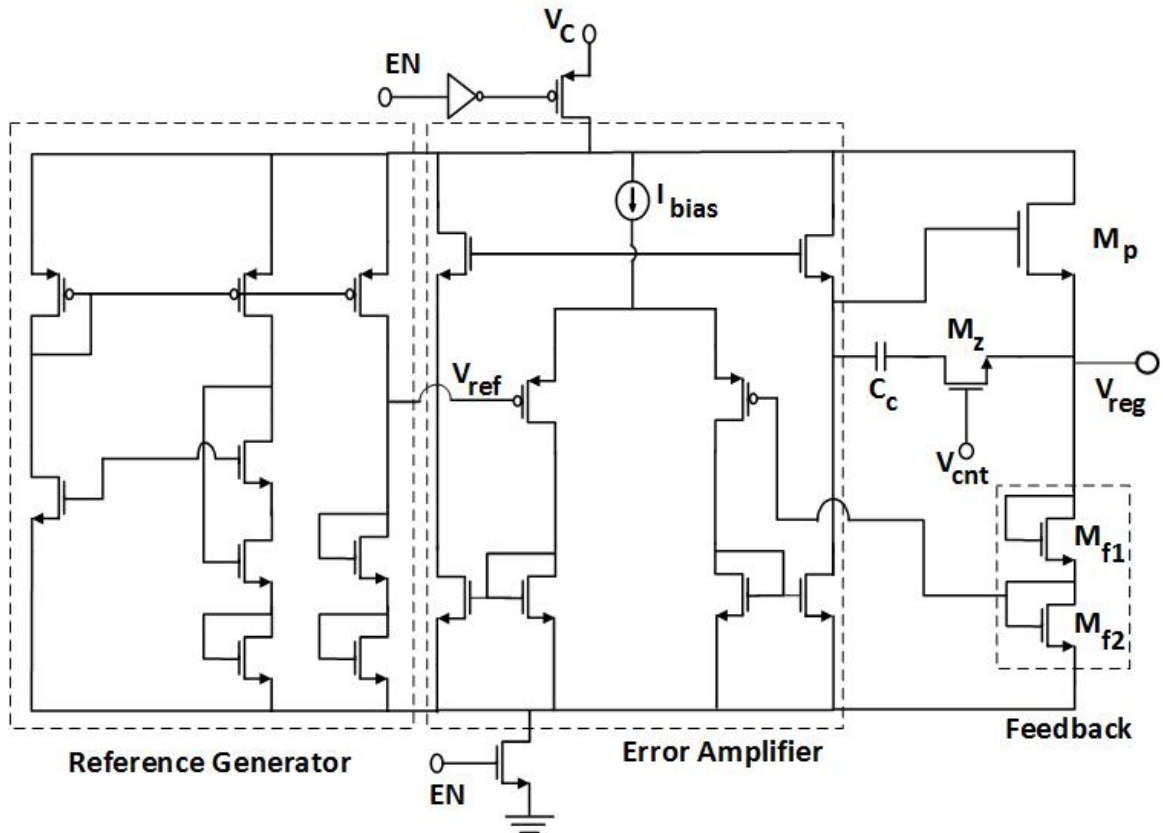


Figure 5.14: The circuit schematic of the voltage regulator.

5.3 Low-noise Amplifier

The neural signals picked up by the penetrated electrodes in the brain are low frequency and have a low amplitude. The spike voltage generated by the action potential of the neurons has an amplitude range of 50–500 μV , and the power spectrum density contains energy within a 300–6 KHz frequency range. Local field potential, on the other hand, has amplitudes up to 5 mV and contains energy even below 1 Hz [47].

Neural signals must be amplified before digitization, since the amplitude is not sufficient and is less than the resolution of a typical ADC. In addition, due to electrochemical interaction between tissue and the electrodes, a DC voltage establishes at the input of amplifiers. Figure 5.15 shows a conceptual view of an amplifier array. More recording nodes are needed to acquire more data from brain activity. The number of recording nodes for a neural recording system that is useful for comprehending the complex dynamics of human cognitive functions could be very large. Therefore, the area and the power consumption of the neural amplifiers play an important role for scalability of the system.

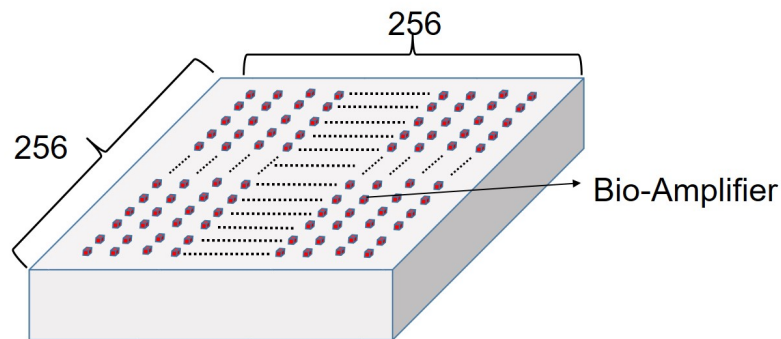


Figure 5.15: A conceptual view of a neural amplifier array that can be used in a neural recording system that is useful for comprehending the dynamics of a complex human cognitive function.

An ultra-low-power neural amplifier is required for an energy-harvesting im-

plantable device. In addition, the area of each amplifier should be minimized as much as possible. Therefore, no off-chip component or large capacitor can be used in the design. In this case, design of the filter needed to block DC signals and pass the frequency component higher than is very challenging. Pseudotransistors that are biased with a voltage close to zero provide a huge resistance and can be used with a typical capacitor that can be implemented on a CMOS process to form a high-pass filter. The cutoff frequency of the filter can be set by the value of the capacitance [48]. The block diagram of a single bio-amplifier is shown in Figure 5.16.

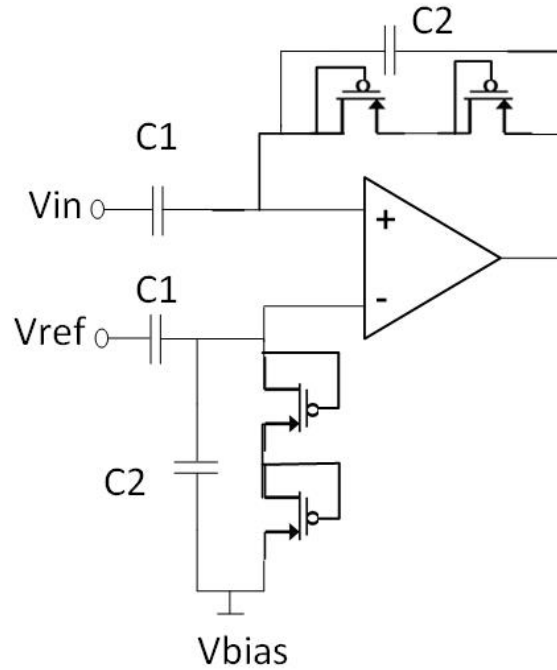


Figure 5.16: The schematic of the low-noise bioamplifier.

The amplifier includes an Operational Transconductance Amplifier (OTA) that provides a high gain. The transistors in the OTA are biased in the sub-threshold region. The current consumption of the OTA is very low, but due to the very high impedance seen at the output node, the gain of the OTA is large and can be used in a feedback loop.

The high-pass filter is implemented using C_2 and the parallel transistor. The overall voltage gain of the amplifier in Figure 5.16 is set by the ratio of $\frac{C_1}{C_2}$. In this design, the values of C_2 and C_1 are selected as 200 fF and 20 pF, respectively. Simulation results show that the amplifier has a gain of 40 dB and has a power consumption of 510 pW when it is powered with a 1 V supply voltage.

5.4 Performance Evaluation

The radiative near-field power harvesting platform is fabricated in 180 nm SOI CMOS process and the micrograph is depicted in Figure 5.17

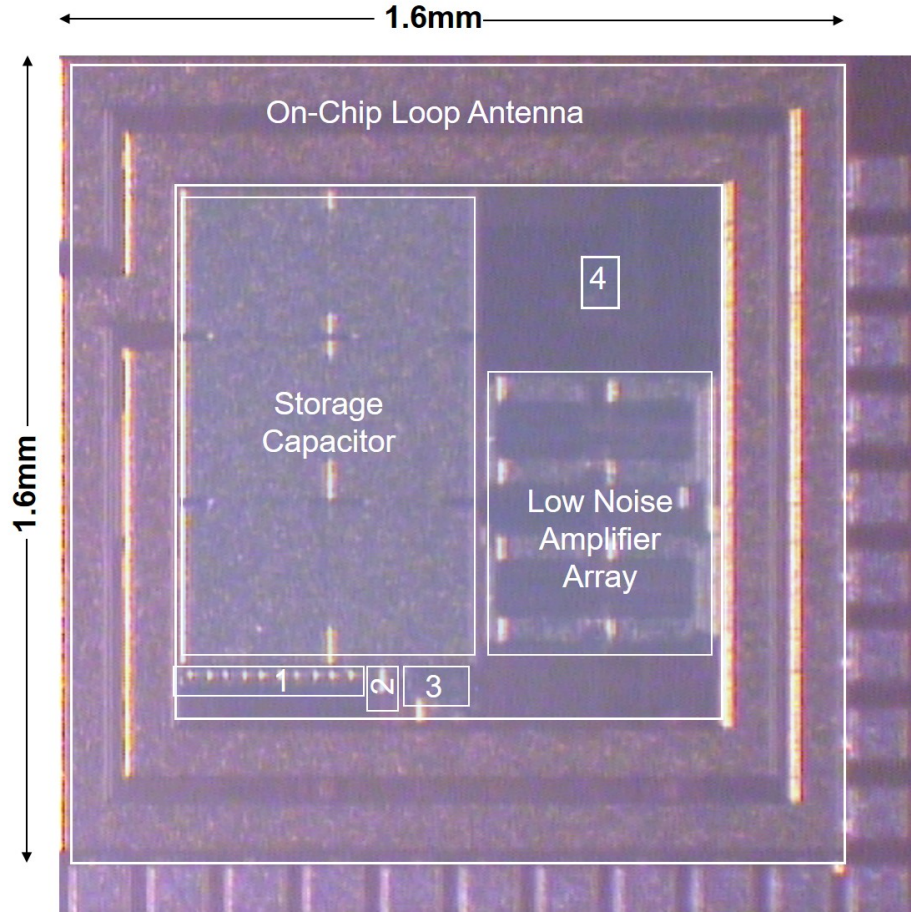
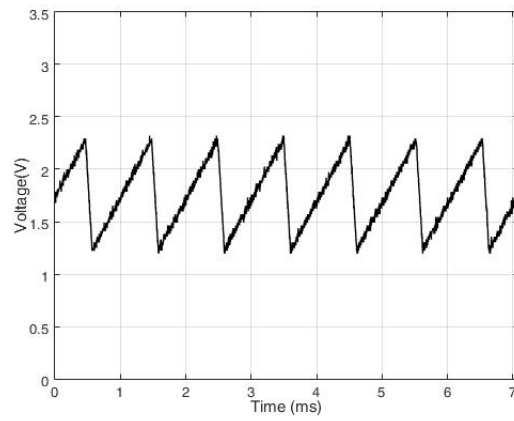


Figure 5.17: A die photo of the wireless power receiver system. 1: Voltage Rectifier, 2: PMU, 3: Voltage Regulator, 4: Reference Generator.

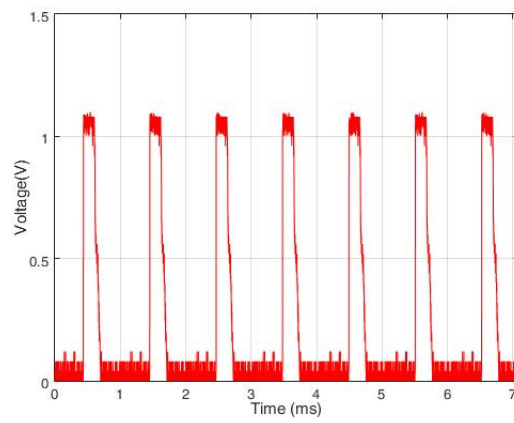
We used a $1 \times 1 \text{ cm}^2$ loop antenna fabricated on a Roger 4353 PCB for transmitting power. The chip was covered by a 1cm-thick chicken breast tissue and it was placed 2cm below the TX antenna. A Keysight E8257D PSG RF source generated the power at 2.75 GHz, wherein the PTE was measured as 26.46 dB for the configuration shown in Figure 4.13. The measurement results show that the power harvesting system is capable of providing up to 1.21 mW for the operation of a high-performance biomedical implant while the amount of transmitted power is under safety limits. The measured waveforms in Figure 5.18 depict different phases of operation and the output voltage of the voltage regulator.

In this measurement, the storage capacitor was increased to 100 nF using an off-chip component to expand the discharging time. In addition, the performances of the voltage rectifier, the PMU, the voltage regulator, and the low noise bio-amplifiers were measured in a stand-alone configuration and are reported in Table 5.1. The current consumption of the entire system in the resting phase is measured as 10 nA, which is 8x smaller than the state-of-the-art [49] work.

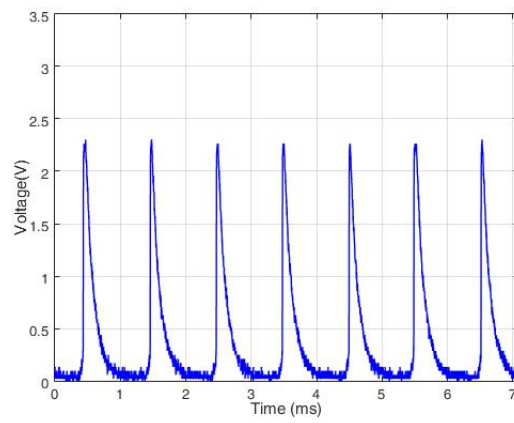
The performance of the fabricated chip was evaluated. Based on the results presented in chapter 6, the wireless link between the transmitting antenna and the chip was characterized and the optimum frequency for wireless power transmission is determined. In addition, the measured parameters of the voltage rectifier, PMU, and voltage regulator are reported in Table 5.1. Some of the design's important features are compared with the most recent published works in Table 5.2.



A



B



C

Figure 5.18: The measured waveform of the voltage across the storage capacitor (V_C), the output voltage of the regulator (V_{reg}), and the EN signal that activates the rest of the system during the discharging phase.

Voltage Rectifier (Six stages)	
<i>Sensitivity*</i> (2V output voltage, 1M Ω load)	-20 dBm
Conversion Efficiency (for a 10 K Ω nominal load)	54 %
Power Management Unit (PMU)	
Threshold Voltages ($V_H - V_L$)	2.34 -1.2 = 1.14 V
Average Current Consumption	10 nA
Maximum Slew Rate for a 1K Ω load	10 mV/ μ s
Voltage Regulator	
Line Regulation	3%
Efficiency (for a 1K Ω load)	45 %
Quiescent Current	10 μ A
Low-noise Amplifiers	
Supply Voltage and Current	1.1V , 2nA V
Gain	39.8 dB V
Bandwidth	49.9 Hz (50 - 0.1 Hz)
Input-referred Noise*	8.4 μ Vrms

* : *Simulated*

Table 5.1: Performance summary of the power harvesting system circuitry.

Reference	This work	[50] IMS'16	[51] IMS'16	[52] TBCS'15	[53] TMTT'13
Technology	0.18 μm SOI CMOS	45 nm SOI CMOS	0.18 μm SOI CMOS	0.13 μ m CMOS	0.18 μ m 2013 CMOS
Area(mm²)	1.6\times1.6	0.43	2.47	2 \times 2.18	3.2 \times 1.5
PMU	Yes	No	Yes	No	Yes
PTE (dB)	-26.46	N/A	N/A	-20.96	N/A
Intermediate Layer	1cm Air, 1cm Chicken Breast	3cm Air, 1cm Chicken Breast	4.2cm Air	10 mm Bovine Muscle	3cm Air, 5mm Saline Solution
On-chip Antenna	Yes	Yes	Yes	Yes	Yes
Frequency (GHz)	2.75	0.915	8-10	0.16	5.2
$P_{out}(\mu W)$	1210	50	N/A	N/A	100
V_{out}	1.1 V regulated	1 V	0.8 V regulated	3.1 V regulated	0.8 V regulated

Table 5.2: Performance comparison of the power harvesting system.

Conclusion

In this thesis, we presented two different power harvesting systems for mm-size implantable application.

A far-field power harvesting platform that is suitable for ultra-low power biomedical implants was presented. All of the components, including the dipole antenna, were implemented on a single silicon chip within 0.42 mm². The operating distance of the system is up to 15 cm, which is the highest reported value compared with previous published works. To the best of author's knowledge, this work reports the first far-field power harvesting system for biomedical implants. In addition, the carrier frequency for power transmission is about 11.2 GHz which is the highest reported carrier frequency for wireless power transfer to implanted biomedical systems. A multi-stage voltage rectifier with a threshold compensation of order 4 was used for AC to DC conversion. The minimum required input power to the rectifier for delivering 1V DC voltage to a 1M Ω resistive load is 23 W, which indicates that this system is useful for powering ultra-low power micro-implants and can be a potential solution for mobile health care devices. The far field power harvesting platform was presented and published in the IEEE Sensors 2016 conference [43].

Another power harvesting platform was presented that can be used for biomed-

ical implants that require high power such as a neural recording systems. A 1.6×1.6 mm² power harvesting platform that operates at 2.75 GHz was presented. The design introduces a power management technique that results in biphasic operation. The fabricated chip is capable of delivering up to 1.21 mW, while the amount of transmitted power is under safety limits. To the best of author's knowledge, it is the highest reported power value among the mm-size power harvesting platforms. The system is resilient to misalignment of the antennas or changes in the type of surrounding biological tissues. The radiative near-field power Harvesting system is going to be presented and published in International Microwave Symposium 2017 [54].

References

- [1] N. Tandon, A. V. Alexopoulos, A. Warbel, I. M. Najm, and W. E. Bingaman, “Occipital epilepsy: spatial categorization and surgical management: clinical article,” *Journal of neurosurgery*, vol. 110, no. 2, pp. 306–318, 2009. 1
- [2] H. Hamer, H. Morris, E. Mascha, M. Karafa, W. Bingaman, M. Bej, R. Burgess, D. Dinner, N. Foldvary, J. Hahn *et al.*, “Complications of invasive video-eeg monitoring with subdural grid electrodes,” *Neurology*, vol. 58, no. 1, pp. 97–103, 2002. 1
- [3] R. P. Lesser, N. E. Crone, and W. Webber, “Subdural electrodes,” *Clinical Neurophysiology*, vol. 121, no. 9, pp. 1376–1392, 2010. 1
- [4] E. Behrens, J. Zentner, D. Van Roost, A. Hufnagel, C. E. Elger, and J. Schramm, “Subdural and depth electrodes in the presurgical evaluation of epilepsy,” *Acta neurochirurgica*, vol. 128, no. 1, pp. 84–87, 1994. 1
- [5] S. S. Spencer, D. D. Spencer, P. D. Williamson, and R. Mattson, “Combined depth and subdural electrode investigation in uncontrolled epilepsy,” *Neurology*, vol. 40, no. 1, pp. 74–74, 1990. 1
- [6] S. S. Spencer, “Depth electroencephalography in selection of refractory epilepsy for surgery,” *Annals of neurology*, vol. 9, no. 3, pp. 207–214, 1981. 1
- [7] K. E. Bouchard, N. Mesgarani, K. Johnson, and E. F. Chang, “Functional organization of human sensorimotor cortex for speech articulation,” *Nature*, vol. 495, no. 7441, pp. 327–332, 2013. 1
- [8] M. K. Leonard and E. F. Chang, “Dynamic speech representations in the human temporal lobe,” *Trends in cognitive sciences*, vol. 18, no. 9, pp. 472–479, 2014. 1
- [9] N. Mesgarani, C. Cheung, K. Johnson, and E. F. Chang, “Phonetic feature encoding in human superior temporal gyrus,” *Science*, vol. 343, no. 6174, pp. 1006–1010, 2014. 1

-
- [10] A. Flinker, E. Chang, N. Barbaro, M. Berger, and R. Knight, "Sub-centimeter language organization in the human temporal lobe," *Brain and language*, vol. 117, no. 3, pp. 103–109, 2011. 1
 - [11] E. Hedegård, J. Bjellvi, A. Edelvik, B. Rydenhag, R. Flink, and K. Malmgren, "Complications to invasive epilepsy surgery workup with subdural and depth electrodes: a prospective population-based observational study," *Journal of Neurology, Neurosurgery & Psychiatry*, pp. jnnp–2013, 2013. 1
 - [12] A. P. Sample, D. J. Yeager, P. S. Powledge, A. V. Mamishev, and J. R. Smith, "Design of an rfid-based battery-free programmable sensing platform," *IEEE Transactions on Instrumentation and Measurement*, vol. 57, no. 11, pp. 2608–2615, 2008. 1
 - [13] A. P. Chandrakasan, N. Verma, and D. C. Daly, "Ultralow-power electronics for biomedical applications," *Annu. Rev. Biomed. Eng.*, vol. 10, pp. 247–274, 2008. 1, 2
 - [14] Q. Zhou, S. Lau, D. Wu, and K. K. Shung, "Piezoelectric films for high frequency ultrasonic transducers in biomedical applications," *Progress in materials science*, vol. 56, no. 2, pp. 139–174, 2011. 1
 - [15] A. I. Hochbaum, R. Chen, R. D. Delgado, W. Liang, E. C. Garnett, M. Najarian, A. Majumdar, and P. Yang, "Enhanced thermoelectric performance of rough silicon nanowires," *Nature*, vol. 451, no. 7175, pp. 163–167, 2008. 1
 - [16] P. P. Mercier, A. C. Lysaght, S. Bandyopadhyay, A. P. Chandrakasan, and K. M. Stankovic, "Energy extraction from the biologic battery in the inner ear," *Nature biotechnology*, vol. 30, no. 12, pp. 1240–1243, 2012. 1
 - [17] J. A. Paradiso and T. Starner, "Energy scavenging for mobile and wireless electronics," *IEEE Pervasive computing*, vol. 4, no. 1, pp. 18–27, 2005. 1
 - [18] S. Priya and D. J. Inman, *Energy harvesting technologies*. Springer, 2009, vol. 21. 2
 - [19] K. N. Bocan and E. Sejdić, "Adaptive transcutaneous power transfer to implantable devices: A state of the art review," *Sensors*, vol. 16, no. 3, p. 393, 2016. 2, 4.6
 - [20] A. B. Amar, A. B. Kouki, and H. Cao, "Power approaches for implantable medical devices," *Sensors*, vol. 15, no. 11, pp. 28 889–28 914, 2015. 2
 - [21] C. A. Balanis, *Antenna theory: analysis and design*. John Wiley & Sons, 2016. 2.1, 4.4.2.1

-
- [22] X. Liu, J. L. Berger, A. Ogirala, and M. H. Mickle, "A touch probe method of operating an implantable rfid tag for orthopedic implant identification," *IEEE Transactions on Biomedical Circuits and systems*, vol. 7, no. 3, pp. 236–242, 2013. 2.1
 - [23] R. Jegadeesan, Y. X. Guo, and M. Je, "Electric near-field coupling for wireless power transfer in biomedical applications," in *2013 IEEE MTT-S International Microwave Workshop Series on RF and Wireless Technologies for Biomedical and Healthcare Applications (IMWS-BIO)*, Dec 2013, pp. 1–3. 2.1
 - [24] M. Kiani and M. Ghovanloo, "The circuit theory behind coupled-mode magnetic resonance-based wireless power transmission," *IEEE Transactions on Circuits and Systems I: Regular Papers*, vol. 59, no. 9, pp. 2065–2074, 2012. 2.1
 - [25] X. Wei, Z. Wang, and H. Dai, "A critical review of wireless power transfer via strongly coupled magnetic resonances," *Energies*, vol. 7, no. 7, pp. 4316–4341, 2014. 2.1
 - [26] A. Karalis, J. D. Joannopoulos, and M. Soljačić, "Efficient wireless non-radiative mid-range energy transfer," *Annals of Physics*, vol. 323, no. 1, pp. 34–48, 2008. 2.1
 - [27] M. Fareq, M. Fitra, M. Irwanto, S. Hasan, and M. Arinal, "Low wireless power transfer using inductive coupling for mobile phone charger," in *Journal of Physics: Conference Series*, vol. 495, no. 1. IOP Publishing, 2014, p. 012019. 2.1
 - [28] A. S. Poon, S. O'Driscoll, and T. H. Meng, "Optimal frequency for wireless power transmission into dispersive tissue," *IEEE Transactions on Antennas and Propagation*, vol. 58, no. 5, pp. 1739–1750, 2010. 2.2, 4.1
 - [29] Y. Ghasempour, N. Prasad, M. Khojastepour, and S. Rangarajan, "Novel combinatorial results on downlink mu-mimo scheduling with applications," in *2017 13th Annual Conference on Wireless On-demand Network Systems and Services (WONS)*, 2017, pp. 1–8. 2.2
 - [30] Y. Ghasempour and E. W. Knightly, "Decoupling beam steering and user selection for scaling multi-user 60 ghz wlans," in *Proceedings of the 18th ACM International Symposium on Mobile Ad Hoc Networking and Computing*. ACM, 2017. 2.2
 - [31] Y. Ghasempour, N. Prasad, M. Khojastepour, and S. Rangarajan, "Link packing in mmwave networks," in *2017 IEEE International Conference on Communications (ICC)*, 2017, pp. 1–7. 2.2
 - [32] "A 'jumper cable' for the brain helps a paralyzed man regain hand movement," <https://www.youtube.com/watch?v=zRgZ0QZ8dRE>, accessed: Apr 13, 2016. 2.2

-
- [33] B. Jamali and A. Babakhani, "A 0.2-2.6 ghz instantaneous frequency-to-voltage converter in 90nm cmos," in *Radio and Wireless Symposium (RWS), 2016 IEEE*. IEEE, 2016, pp. 45–47. 2.2
 - [34] D. M. Pozar, "Microwave engineering 3e," *Transmission Lines and Waveguides*, pp. 143–149, 2005. 2.2
 - [35] M. Seok, G. Kim, D. Blaauw, and D. Sylvester, "A portable 2-transistor picowatt temperature-compensated voltage reference operating at 0.5 v," *IEEE Journal of Solid-State Circuits*, vol. 47, no. 10, pp. 2534–2545, 2012. 3.1
 - [36] S. J. Orfanidis, *Electromagnetic waves and antennas*. Rutgers University New Brunswick, NJ, 2002. 4.1, 4.2
 - [37] A. Drossos, V. Santomaa, and N. Kuster, "The dependence of electromagnetic energy absorption upon human head tissue composition in the frequency range of 300-3000 mhz," *IEEE transactions on microwave theory and techniques*, vol. 48, no. 11, pp. 1988–1995, 2000. 4.3
 - [38] H. Bahrami, S. A. Mirbozorgi, L. A. Rusch, and B. Gosselin, "Biological channel modeling and implantable uwb antenna design for neural recording systems," *IEEE Transactions on Biomedical Engineering*, vol. 62, no. 1, pp. 88–98, 2015. 4.3
 - [39] J. S. Ho, A. J. Yeh, E. Neofytou, S. Kim, Y. Tanabe, B. Patlolla, R. E. Beygui, and A. S. Poon, "Wireless power transfer to deep-tissue microimplants," *Proceedings of the National Academy of Sciences*, vol. 111, no. 22, pp. 7974–7979, 2014. 4.3
 - [40] C. Gabriel, S. Gabriel, and E. Corthout, "The dielectric properties of biological tissues: I. literature survey," *Physics in medicine and biology*, vol. 41, no. 11, p. 2231, 1996. 4.3
 - [41] C. Nguyen and J. Park, "General analysis of radar sensors," in *Stepped-Frequency Radar Sensors*. Springer, 2016, pp. 9–38. 4.4.2.1
 - [42] G. Papotto, F. Carrara, and G. Palmisano, "A 90-nm cmos threshold-compensated rf energy harvester," *IEEE Journal of Solid-State Circuits*, vol. 46, no. 9, pp. 1985–1997, 2011. 5.1.1, 5.1.1
 - [43] H. Rahmani and A. Babakhani, "A fully integrated electromagnetic energy harvesting circuit with an on-chip antenna for biomedical implants in 180 nm soi cmos," in *SENSORS, 2016 IEEE*. IEEE, 2016, pp. 1–3. 5.1.3, 6
 - [44] B. Gurakan, O. Ozel, J. Yang, and S. Ulukus, "Energy cooperation in energy harvesting communications," *IEEE Transactions on Communications*, vol. 61, no. 12, pp. 4884–4898, 2013. 5.2.1

-
- [45] S. Mandal and R. Sarpeshkar, “Low-power cmos rectifier design for rfid applications,” *IEEE Transactions on Circuits and Systems I: Regular Papers*, vol. 54, no. 6, pp. 1177–1188, 2007. 5.2.1
 - [46] S. O’Driscoll, A. S. Poon, and T. H. Meng, “A mm-sized implantable power receiver with adaptive link compensation,” in *Solid-State Circuits Conference-Digest of Technical Papers, 2009. ISSCC 2009. IEEE International*. IEEE, 2009, pp. 294–295. 5.2.1
 - [47] R. R. Harrison, P. T. Watkins, R. J. Kier, R. O. Lovejoy, D. J. Black, B. Greger, and F. Solzbacher, “A low-power integrated circuit for a wireless 100-electrode neural recording system,” *IEEE Journal of Solid-State Circuits*, vol. 42, no. 1, pp. 123–133, 2007. 5.3
 - [48] R. R. Harrison and C. Charles, “A low-power low-noise cmos amplifier for neural recording applications,” *IEEE Journal of solid-state circuits*, vol. 38, no. 6, pp. 958–965, 2003. 5.3
 - [49] G. Papotto, F. Carrara, A. Finocchiaro, and G. Palmisano, “A 90-nm cmos 5-mbps crystal-less rf-powered transceiver for wireless sensor network nodes,” *IEEE Journal of Solid-State Circuits*, vol. 49, no. 2, pp. 335–346, 2014. 5.4
 - [50] A. Y.-S. Jou, H. Pajouhi, R. Azadegan, and S. Mohammadi, “A cmos integrated rectenna for implantable applications,” in *Microwave Symposium (IMS), 2016 IEEE MTT-S International*. IEEE, 2016, pp. 1–3. ??
 - [51] Y. Sun and A. Babakhani, “A wirelessly powered injection-locked oscillator with on-chip antennas in 180nm soi cmos,” in *Microwave Symposium (IMS), 2016 IEEE MTT-S International*. IEEE, 2016, pp. 1–3. ??
 - [52] M. Zargham and P. G. Gulak, “Fully integrated on-chip coil in 0.13 μ cmos for wireless power transfer through biological media,” *IEEE transactions on biomedical circuits and systems*, vol. 9, no. 2, pp. 259–271, 2015. ??
 - [53] M. H. Ouda, M. Arsalan, L. Marnat, A. Shamim, and K. N. Salama, “5.2-ghz rf power harvester in 0.18 μ m cmos for implantable intraocular pressure monitoring,” *IEEE Transactions on Microwave Theory and Techniques*, vol. 61, no. 5, pp. 2177–2184, 2013. ??
 - [54] H. Rahmani and A. Babakhani, “A wireless power receiver with an on-chip antenna for millimeter-size biomedical implants in 180 nm soi cmos,” in *Microwave Symposium (IMS), 2017 IEEE MTT-S International*. IEEE, 2017, pp. 1–4. 6